

Back from the dead: AT2019aalc as a candidate repeating TDE in an AGN

Patrik Milán Veres¹, Anna Franckowiak^{1,2}, Sjoert van Velzen³, Bjoern Adebahr¹, Sam Taziaux¹, Jannis Necker^{4,5}, Robert Stein⁶, Alexander Kier¹, Ancla Müller¹, Dominik J. Bomans^{1,2}, Nuria Jordana-Mitjans¹, Marek Kowalski⁴, Erica Hammerstein^{7,8,9}, Elena Marci-Boehncke¹, Simeon Reusch^{4,5}, Simone Garrappa¹⁰, Sam Rose⁶, and Kaustav Kashyap Das¹¹

- ¹ Ruhr University Bochum, Faculty of Physics and Astronomy, Astronomical Institute (AIRUB), Universitätsstraße 150, 44801 Bochum, Germany e-mail: veres@astro.ruhr-uni-bochum.de
- ² Ruhr Astroparticle and Plasma Physics Center (RAPP Center)
- ³ Leiden Observatory, Leiden University, Postbus 9513, 2300 RA Leiden, The Netherlands
- ⁴ Deutsches Elektronen-Synchrotron (DESY), Platanenallee 6, D-15378 Zeuthen, Germany
- ⁵ Institut für Physik, Humboldt-Universität zu Berlin, D-12489 Berlin, Germany
- ⁶ Division of Physics, Mathematics, and Astronomy, California Institute of Technology, Pasadena, CA 91125, USA
- ⁷ University of Maryland, Department of Astronomy, 4296 Stadium Dr, College Park, MD 20742, USA
- ⁸ NASA Goddard Space Flight Center, Astrophysics Science Division, 8800 Greenbelt Rd, Greenbelt, MD 20771, USA
- ⁹ Center for Research and Exploration in Space Science and Technology, NASA/GSFC, Greenbelt, MD 20771, USA
- ¹⁰ Department of Particle Physics and Astrophysics, Weizmann Institute of Science, 76100 Rehovot, Israel.
- ¹¹ Cahill Center for Astrophysics, California Institute of Technology, MC 249-17, 1200 E California Boulevard, Pasadena, CA, 91125, USA

ABSTRACT

Context. To date, three nuclear transients have been associated with high-energy neutrino events. These transients are generally thought to be powered by tidal disruptions of stars (TDEs) by massive black holes. However, AT2019aalc, hosted in a Seyfert-1 galaxy, was not yet classified due to a lack of multiwavelength observations. Interestingly, the source has re-brightened 4 years after its discovery.

Aims. We aim to classify the transient and explain the mechanism responsible for its second optical flare.

Methods. We conducted a multi-wavelength monitoring program (from radio to X-rays) of AT2019aalc during its re-brightening in 2023.

Results. The observations revealed a uniquely bright UV counterpart and multiple X-ray flares during the second optical flaring episode of the transient. The second flare, similarly to the first one, is also accompanied by IR dust echo emission. A long-term radio flare is found with an inverted spectrum. Optical spectroscopic observations reveal the presence of Bowen Fluorescence lines and strong high-ionization coronal lines indicating an extreme level of ionization in the system.

Conclusions. The results suggest that the transient can be classified as a Bowen Fluorescence Flare (BFF), a relatively new sub-class of flaring active galactic nuclei (AGN). AT2019aalc can be also classified as an extreme coronal line emitter (ECLE). We found that, in addition to AT2019aalc, another BFF AT2021loi is spatially coincident with a high-energy neutrino event. The multi-wavelength properties of these transients suggest a possible connection between ECLEs, BFFs and TDEs in AGN.

Key words. galaxies: active – galaxies: Seyfert – quasars: emission lines – individual: AT2019aalc – Neutrinos

1. Introduction

Tidal disruption events (TDEs) are rare transient events, which occur when a star approaches a supermassive black hole (SMBH) and the tidal forces of the latter rip the star apart (Rees 1988). About half of the star’s material is accreted around the black hole, generating a luminous outburst across the electromagnetic spectrum. Despite most of these transient sources have been discovered by optical telescopes, the origin of their optical/UV emission is poorly understood. One model is colliding stellar debris stream shocks (Piran et al. 2015). Another scenario is reprocessed soft X-ray/far UV emission (originating from the debris accretion onto the black hole) by an extended elliptical disk, or an envelope, or an outflow surrounding the central debris disk (for a recent review see Bu et al. 2022). TDE optical light curves are characterized by quick and colorless evolving but also

fast (on monthly timescales) decaying optical emission. Several TDEs were detected in X-rays with a very soft X-ray spectrum typically explained by late-time accretion disk formation (Saxton et al. 2020). In addition, a handful of TDEs produced detectable radio emission, explained by delayed¹ non-relativistic outflows (Horesh et al. 2021; Cendes et al. 2023), or only in 4 instances by newly launched relativistic on-axis jets (Berger et al. 2012; Brown et al. 2015; Cenko et al. 2012; De Colle & Lu 2020; Yao et al. 2023a). Spectroscopically, TDEs are characterized by a strong blue continuum and broad emission lines ($> 10^4$ km s⁻¹) e.g., H α and H β . As the photosphere shrinks over time, the flux of the ionized lines such as He II 4686Å tend to increase while the He II/H α ratio increases (e.g., Hung et al. 2017; Charalam-

¹ Note that the SMBH accretion rate does not peak on the same timescale as the mass fall-back rate.

popoulos et al. 2022a) and, in a few cases, Bowen Fluorescence (BF; Bowen 1934, 1935) lines e.g., N III at 4640Å appear (e.g., Blagorodnova et al. 2019; Charalampopoulos et al. 2022a).

To date, roughly 120 promising candidate TDEs are known. However, since most of the above-mentioned observed properties do not exclusively characterize TDEs, spectroscopic coverage is required to distinguish TDEs from ‘TDE impostors’ such as conventionally accreting active galactic nuclei (AGN), changing-look AGN (CLAGN), supernovae (SNe) or even stellar collisions (Zabludoff et al. 2021).

TDEs generally result in one optical flare, however, in a few cases a re-brightening episode (or episodes) was detected even years after the initial flare. These might be explained in the following way. Under special circumstances, a star on a grazing orbit might be partially disrupted and only a fraction of the stellar mass will be deposited onto the SMBH. The secondary disruption of a surviving core after it reaches the pericenter again results in X-ray re-brightening explained by renewed accretion. The first systematically identified repeating partial TDE, AT2020vdq, has been classified after simultaneous multi-wavelength monitoring (Somalwar et al. 2023). Only a few other partial TDEs or candidates are known to date, these are ASASSN 14ko (Payne et al. 2021); eRASSt J045650.3-203750 (Liu et al. 2023); RX J133157.6-324319.7 (Hampel et al. 2022); AT2018fyk (Wevers et al. 2019a, 2023); AT2019avd (Chen et al. 2022) and AT2022dbl (Lin et al. 2024).

Based on the observed properties of TDE host galaxies, French et al. (2020) estimated a TDE rate of 10^{-5} per year per galaxy which is well borne out by recent data (Yao et al. 2023b). Importantly, a similar fraction of TDEs should take place in AGN hosts (e.g., Chan et al. 2019; Ryu et al. 2024). The multi-wavelength characteristics of such a TDE should clearly differ from the ones taken place in quiescent galaxies, as the AGN is surrounded by a pre-existing accretion disk. Due to the extreme difference in density between the two, neither the star nor the accretion disk are affected after the first passage through the disk. However, the confined debris stream has such a low density after the star is tidally disturbed that when it interacts with the disk the collision between the stream and the disk can potentially dissipate much of the kinetic energy possessed by the stream and the disk gas near the impact point, and it can be radiated away (Chan et al. 2019). These transients are challenging to distinguish from AGN variability. Only a few candidate TDEs taken place in AGN (in the following: TDE-AGN) were studied earlier (e.g., PS16dtm - a TDE in a Narrow-Line Seyfert-1 (NLSy1) galaxy (Blanchard et al. 2017) or the multiple soft X-ray flares in IC 3599 (Campana et al. 2015) and GSN 069 (Shu et al. 2018)). In contrast with TDEs seen in earlier quiescent galaxies, these transients are characterized by slowly decaying optical emission and bumps tend to appear after the peak.

The family tree of AGN-related transients became much broader in the past years (e.g., Frederick et al. 2021). In addition to TDEs, flaring NLSy1s, CLAGN and different types of SNe were classified as typical nuclear transients. Recently, Trakhtenbrot et al. (2019) identified a new class of flares from accreting SMBHs. In 2019, the transient events AT2017bgt, F01004-2237 and OGLE17aaj have been identified as the first members of the class based on their unique optical spectroscopic features. Later, the peculiar X-ray loud transient AT2019avd (Trakhtenbrot et al. 2020) was found with remarkable common properties, however, its classification as an AT2017bgt-like transient is unclear. A more promising case is AT2021loi (Makrygianni et al. 2023), a UV-bright transient event with very similar multi-wavelength properties to the 3 instances studied by Trakhtenbrot

et al. (2019). Those show unobscured AGN-like optical spectra with significant and persistent BF lines, extremely strong UV emission and slowly, on yearly scales, decaying optical emission. These AGN are characterized by significantly and longer-term intensified accretion and might be powered by a binary TDE or an interaction between an outflow and the broad-line region (BLR) or binary SMBHs (Trakhtenbrot et al. 2019). Notably, these transients take place in different types of AGN; AT2017bgt and OGLE17aaj in narrow-line AGN, AT2021loi in a broad-line AGN, F01004-2237 in an ultra-luminous infrared galaxy (ULIRG) while AT2019avd occurred in an earlier quiescent galaxy. Hereafter, we will refer to this new class of AGN flares as Bowen Fluorescence Flares (BFFs), following Makrygianni et al. (2023). Using the Zwicky Transient Facility (ZTF, Masci et al. 2019) Public Survey data, Dgany et al. (2023) found only one BFF candidate (AT2021seu) among 223 spectroscopically classified transients, suggesting that these flares are rare. Other candidates, namely VT J1548 (Somalwar et al. 2022) and AT2022fpx, (Koljonen et al. 2024) were found recently.

In recent years, two nuclear transients were found to be spatially coincident with neutrino events detected by the IceCube Neutrino Observatory based on ZTF follow-up campaigns of IceCube neutrino alerts (Stein et al. 2023). The TDE AT2019dsg is likely associated with the IceCube neutrino, IC191001A (Stein et al. 2021) and a further promising association, between the candidate TDE AT2019fdr and the IceCube neutrino IC200530A (Reusch et al. 2022) points to TDEs as a potential new class of sources of the extragalactic neutrinos. Both sources were found to have unusually luminous mid-infrared emission, and a search for similar flares (van Velzen et al. 2024) led to the identification of the transient event AT2019aalc (a.k.a. ZTF19aaejtoy) with the neutrino alert IC191119A (see Sect. 2. for explanation).

In this paper, we focus on the nuclear transient event and neutrino source candidate AT2019aalc especially on its significant optical re-brightening that has started 4 years after its initial flare (Veres et al. 2023).

We conducted multi-wavelength observations (from radio to X-rays) during the re-brightening and compare it to the initial flare associated with the high-energy neutrino, with the aim to characterize the multi-wavelength properties of this unusual transient event and to classify it.

The paper is organized as follows. We explain the discovery of the transient event and give an insight about its host galaxy in Sect. 2, we summarize our observing campaign and the data reduction in Sect. 3, we present the results of the observations in Sect. 4 and discuss them in Sect. 5 and finally give a summary and conclude in Sect. 6. Throughout the paper, we adopt a flat Λ CDM cosmological model with parameters $H_0 = 70 \text{ km s}^{-1} \text{ Mpc}^{-1}$, $\Omega_\Lambda = 0.73$, and $\Omega_m = 0.27$. In this model (Wright 2006), 1 mas angular size corresponds to 0.72 pc projected linear size at the source redshift $z = 0.0356$ (Ahn et al. 2012). This redshift corresponds to a luminosity distance of 158.3 Mpc. All magnitudes are given in AB system (Oke 1974).

2. The transient event: AT2019aalc

Studying the infrared properties of AT2019dsg and AT2019fdr have revealed a strong reverberation signal i.e. the infrared dust echo, known as reprocessed emission of optical/UV photons in the infrared by hot dust around the SMBH, at a distance of 0.1 – 1 pc (Dou et al. 2016; Lu et al. 2016; van Velzen et al. 2021b, 2024). In addition to the exceptionally high infrared luminosities (due to the infrared echo) of these transients, the neutrino detection times appear to be temporally consistent with the

infrared luminosity peaks (Stein et al. 2021; Reusch et al. 2022). This discovery motivated a systematic search for neutrino emission using an extended sample of black hole flares (van Velzen et al. 2024). This archival search revealed the nuclear transient AT2019aalc with a powerful optical flare and dust echo emission in spatial coincidence with the high-energy neutrino event, IC-191119A (IceCube Collaboration 2019) detected by the IceCube Observatory.

The host galaxy of AT2019aalc (2MASX J15241665+0451192) is a barred spiral (SBa) galaxy hosting an active nucleus (Oh et al. 2013). Based on its Sloan Digital Sky Survey (SDSS; Abazajian et al. 2009) spectrum it was further classified as a broad-line Seyfert-1 galaxy (Trump et al. 2013; Liu et al. 2019). The galaxy was detected in archival radio sky surveys e.g., the Very Large Array Faint Images of the Radio Sky at Twenty-cm (VLA FIRST; Condon et al. 1998). Fig. 1 shows the Pan-STARRS (Chambers et al. 2016) i-band optical image of the host galaxy together with the contours of the FIRST radio data (at 1.4 GHz) and the position of the X-ray counterpart detected by *Swift*/XRT in 2023/2024. The host galaxy is not present in any X-ray catalogs prior to the optical discovery of the transient in 2019.

In addition to the unusually significant infrared echo, AT2019aalc shares multi-wavelength characteristics with the two other neutrino candidate transient events: a soft X-ray spectrum and transient radio emission (van Velzen et al. 2024). Moreover, similar to the other two instances, the infrared peak of the transient event is temporarily coincident with the detection time of the likely associated neutrino event. Notably, Winter & Lunardini (2023) estimated the highest neutrino fluence for AT2019aalc, due to its high estimated SMBH mass ($M_{\text{BH}} = 10^{7.2} M_{\odot}$, van Velzen et al. 2024) and low redshift ($z = 0.0356$, Ahn et al. 2012).

Since the proposed association with the high-energy neutrino event was announced roughly 2 years after the discovery of the transient event, the source was not at the focus of attention or being directly monitored at the time when the neutrino was emitted. Thus, the lack of spectroscopic monitoring during the first optical flare hindered a clear classification of the event. Nevertheless, out of the more than 10^4 AGN detected by the ZTF, less than 1% show similarly rapid and large outbursts (Reusch et al. 2022; van Velzen et al. 2024) suggesting a very unusual AGN case. The TDE-characteristic evolution of the blackbody light curve including a large and rapid optical flux increase is compatible with a TDE-related scenario. However, due to the host galaxy classification, extreme AGN variability provides an alternative explanation for the transient event.

Interestingly, roughly 4 years after the first flare, a significant optical re-brightening started in mid-May 2023 (Veres et al. 2023), illustrated by the long-term ZTF difference light curve shown in Fig. 2. Although double-peaked optical light curves could be a quasi-universal signature of TDEs around massive ($> 10^7 M_{\odot}$) black holes (Wevers et al. 2019b), such a long double peaked light curve with two comparable peak magnitudes would be very untypical for a regular TDE. Throughout this paper we will discuss the results of our observations taken around and after the peak of the second optical flare in the light of different TDE,- and AGN-related scenarios.

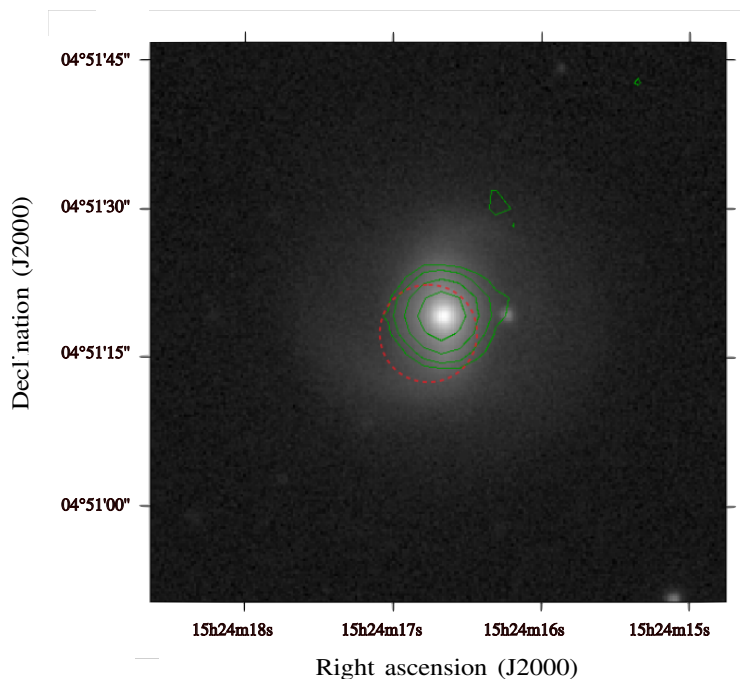


Fig. 1. Pan-STARRS i-band image centered on the host galaxy position of the transient event AT2019aalc. The object located to the west of the galaxy core is a foreground star. The green contours represent the FIRST radio observations taken at 1.4 GHz. The lowest contour level is drawn at 3σ image noise level corresponding to $0.4 \text{ mJy beam}^{-1}$. Additional positive contour levels increase by a factor of 2. The peak brightness is $5.8 \text{ mJy beam}^{-1}$. The red circle points to the *Swift*-XRT 0.3 – 10 keV astrometrically-corrected position, determined using the *Swift*-XRT data products generator (Evans et al. 2014). Its size indicates the 90% confidence positional error.

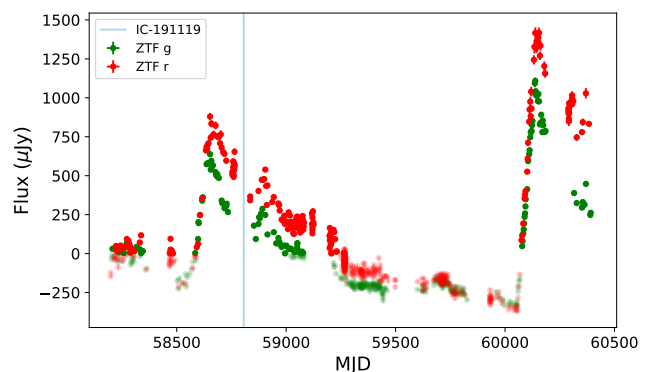


Fig. 2. Optical light curve of AT2019aalc based on ZTF difference photometry. The transparent markers indicate negative flux i.e. the flux decreased below the mean flux of the reference images. Two distinct flares can be seen. The second flare peaked 4 years after the first one and is still ongoing. The blue vertical line indicates the arrival time of the neutrino event IC-191119 associated with the transient.

3. Observations and data reduction

3.1. Optical/UV

3.1.1. ZTF

ZTF forced photometry at the location of AT2019aalc was obtained following the recommendations outlined in Masci et al.

(2023). We corrected for extinction with adopting a galactic extinction of $E(B - V) = 0.039$ (Schlafly & Finkbeiner 2011). As shown in Fig. 2, the forced photometry yields a negative flux in the period between the two flares (and also just before the first flare). This implies that during these epochs, the flux decreased below the mean flux of the reference images. For the r -band these were obtained in between March and May, 2018. While the baseline used to obtain the difference flux of the g -band is based on images obtained between March and September, 2018.

3.1.2. UVOT

The *Neil Gehrels Swift Observatory* (Arnaud 1996a) performed 25 Target of Opportunity (ToO) observations (project codes: 18972 and 19188, Proposers: Reusch, Veres& Sniegowska) on AT2019aal from 2023-06-23 to 2024-05-27 with a total exposure time of 33130 ks. The Ultraviolet and Optical Telescope (UVOT, Roming et al. 2005) onboard the satellite observed the target field with the following four filters in each epoch: UW2 (central wavelength, 1928 Å), UVM2 (2246 Å), UW1 (2600 Å) and U (3465 Å). We analyzed the UVOT images using the *Swift* UVOT tools included in the HEASOFT 6.30 software package. We measured the flux using UVOTSOURCE, applying a circular aperture of 15 arcseconds (which capture nearly all the flux of the host galaxy). The background was measured using four 6 arcsecond regions in four quadrants away from the host galaxy. To estimate the UV flux before the flare, we use GALEX (Martin et al. 2005) observations obtained in 2007 and 2011. We use the same 15" circular aperture that was applied to the *Swift*/UVOT observations and use the GPHOTON software (Million et al. 2016) to extract the flux. Over the 4 year baseline the GALEX observations, the NUV magnitudes change by about 0.3 mag. Following van Velzen et al. (2021a), we combine the mean GALEX flux with the SDSS (York et al. 2000) magnitudes and apply Prospector (Johnson & Leja 2017) to find the best-fit stellar population synthesis model (Conroy et al. 2009) that describes these data. From this model we estimate the baseline flux in the UVOT filters and this baseline is subtracted to obtain the difference flux. Finally, we corrected for galactic dust extinction for each filter.

The baseline flux in the UVM2 band is 17.2, implying a flux increase of 1.8 mag relative to the peak of the UVM2 light curve. This large flux increase implies that, at the peak of the flare, we are not sensitive to the value of the baseline flux. This is useful because the baseline of the ZTF forced photometry was obtained around 2018 (at the start of the ZTF survey), while the baseline that is used to obtain the UVOT difference flux is mainly determined by the GALEX observations that were obtained a decade earlier.

3.2. Infrared

The Palomar 200-inch (P200) near-infrared telescope equipped with the Wide Field Infrared Camera (WIRC, Wilson et al. 2003) observed AT2019aal on 2023-07-05. The imaging was obtained in the J-, H-, and Ks-bands. The data was processed with the SWARP software (Bertin et al. 2002). We performed background subtraction using the PHOTUTILS.BACKGROUND class and measured the flux using a circular aperture with a radius of 9 pixels. The corresponding zero-point magnitudes for this aperture size were calculated using the automatic pipeline for each filter. The error bars are the computed Poisson and background error of the

photometry² and we also took into account the uncertainty of the derived zero-point magnitudes. Finally, we corrected for galactic dust extinction.

We obtained mid-infrared photometry from archival observations of the Wide-Field Survey Explorer (WISE, Wright et al. 2010), which is continuously monitoring the sky at 3.4 μm (W1) and, due to the NEOWISE project (Mainzer et al. 2011), at 4.6 μm (W2). It visits any point in the sky roughly every six months for about ten times. Using timewise (Necker & Mechal 2024; Necker et al. 2024), we downloaded all available multi-epoch photometry data from the AllWISE data release and single-epoch photometry from the NEOWISE-R data releases and stacked the data per visit to obtain robust measurements. All selected single-exposure photometry data points are within 1 arcsecond of the nucleus of the host. The resulting light curve spans almost 14 years, starting in February 2010 until July 2023.

3.3. X-ray

The *Swift*'s X-ray Telescope (XRT, Burrows et al. 2005) observations were obtained simultaneously with the UVOT observations. The observations were performed in photon counting (PC) mode. For each of the epochs, we performed the data reduction using the Space Science Data Center (SSDC) interactive archive in the following way. First, cleaned event-files were produced using the XRTPipeline task. The exposure map, used to correct for the loss of flux caused by some of the CCD pixels not being used to collect data, was created with the XRTEXPOMAP tool. The XIMAGE tool allowed us to determine the source detection level and the source position. In case of non-detections, 3σ upper limits for the count rate were derived and converted to flux using the WebPIMMS³ tool and assuming the mean power-law index of the observations yielded in detections. When our target source was detected above the 3σ level, we ran the SWXRTDAS tool in order to extract the source and the background spectra. Source counts were retrieved from a circle with a radius of 20 pixel (47 arcseconds), while background counts were extracted using an annular region with 80/120 pixel inner/outer radius. In addition, Ancillary Response Files (ARFs) i.e. effective response files for the extracted spectra and Response Matrices Files (RMF), that are used to link the instrumental channel scale with the physical wavelength scale, were automatically created. Finally, the GRPPHA tool of the HEASOFT 6.32 software package was used to perform background subtraction using the source and background spectra and to create a readable spectrum for spectral fitting tools. The relevant ARF and RMF files were applied during this step. We rebinned each spectrum to have a minimum of 3 counts per spectral bin. Channels below 0.3 keV were ignored.

We fitted the individual X-ray spectra using the XSPEC fitting environment (Arnaud 1996b) in order to be able to study the X-ray flux evolution of AT2019aal. First, we have determined the needed Galactic neutral hydrogen column density, N_{H} , based on the HI4PI survey (HI4PI Collaboration et al. 2016). Then, we loaded the source spectrum and converted the instrumental Channel scale to 'physical' wavelength scale. The spectrum was then fitted using Cash-statistic (C-stat, Cash 1976). To find the best-fitting model, we first fitted the stacked spectrum with a ab-

² <https://www.stsci.edu/hst/instrumentation/wfc3/data-analysis/photometric-calibration/ir-photometric-calibration>

³ <https://heasarc.gsfc.nasa.gov/cgi-bin/Tools/w3pimms/w3pimms.pl>

sorbed power-law (`TBABS*POWERLAW` in XSPEC) model as most of the AGN are dominated by a simple power-law and the last XMM data of AT2019aalc before our monitoring program was best-fit with a power-law model (Pasham 2023). We performed renormalization and ignored bad data points. When fitting the model, the galactic column density was fixed whilst the power-law index and the normalization were free to vary. The resultant fit quality is $C\text{-Stat} = 161.49$ for 168 degrees of freedom. We then added a blackbody model component, to take into account the soft excess. The blackbody temperature and the normalization of the new component were also free to vary and we fitted again which resulted in a better fit with $C\text{-Stat} = 149.0$ for 166 degrees of freedom. We implemented the likelihood ratio test (`lrt` in XSPEC) to estimate the statistical significance of the inclusion of the blackbody component. This test runs a given number of simulations of datasets based on the two models provided (which are the simple power-law and the more complex power-law+blackbody models in our case) and calculates the likelihood ratio for the more complex model relative to the simpler one. After running 100 simulations, the test resulted only in smaller likelihood differences than the observed one (≈ 12) clearly implying that the difference is unlikely to be due to random fluctuations. Therefore, accounting for the soft X-ray excess results in a significantly better fit than a normal power-law fit to model the stacked spectrum. The source luminosity of each dataset was determined with adding the `CLUMIN` component in front of the model components. We fixed the normalization in the additive models (power-law and blackbody) and performed the fit again. Finally, we derived the 90% confidence level (2.706) error of the luminosity and the power-law index and, when it was relevant, the blackbody temperature. When fitting the individual datasets, a simple power-law model was enough to adequately describe the data and the soft excess becomes significant only in the stacked spectrum. Only one of the individual datasets is better fit with a blackbody model than with a power-law+blackbody or a simple power-law models.

3.4. Radio

3.4.1. VLBI observations

We observed AT2019aalc with the European VLBI Network (EVN) and the enhanced Multi-Element Remotely Linked Interferometer Network (e-MERLIN, Garrington et al. 2004). Our very long baseline interferometry (VLBI) maps enable us to study the pc-scale radio structure of AT2019aalc. These observations were carried out at 1.7 GHz (L-band) on 2023 June 09 (project code: EV027, PI: Veres). Each of the eight intermediate-frequency channels (IFs) were divided into thirty-two 500 kHz spectral channels, resulting in a total bandwidth of 128 MHz. The whole observation time was 10 hr. The experiment was performed in phase-referencing mode with 5-min duty cycles (with spending 3.5 min on the target during each cycle) which resulted in an on-source time of 6.7 h including fringe-finder scans and slewing. The following 15 antennas participated in the observations: Cm: Cambridge, UK; Da: Darnhall, UK; De: Defford, UK, Ef - Effelsberg, Germany; Hh - Hartebeesthoek, South Africa; Jb - Jodrell Bank Mk2, UK; Kn - Knockin, UK; MC - Medicina, Italy; Pi - Pickmere, UK; O8 - Onsala, Sweden; T6 - Tianma, China; Tr - Toruń, Poland; Ur - Urumqi, China; Wb - Westerbork, The Netherlands. The data were recorded in left and right circular polarizations with a data rate of 1 Gbit s^{-1} . The correlation was done at the EVN Data Processor (Keimpema et al. 2015) at the Joint Institute for VLBI European Research In-

frastructure Consortium (Dwingeloo, The Netherlands) with an averaging time of 2 s. The Compact Symmetric Object (CSO) 1521+0430 (a.k.a. 4C 04.51) at an angular distance of 0.83° was observed as phase-reference calibrator. Earlier EVN observations of this calibrator source taken at 1.7 GHz resolved two lobes, with a hint of a jet-like emission (Xiang et al. 2002). In addition, the following radio sources were observed as fringe-finders: J1430+1043, J1550+0527 and J1751+0939. The bright CSO J1407+2827 (a.k.a. OQ208) was observed as amplitude calibrator and in order to calibrate the Merlin antennas properly.

The data were calibrated with the U.S. National Radio Astronomy Observatory Astronomical Image Processing System (AIPS, Greisen 1990) software package following the standard procedures. We performed time flagging using the `.uvflag` ancillary table. The amplitude calibration has been done using the measured system temperatures⁴ and gain curves of each telescope contained in the `.antab` ancillary table. Since our observations were conducted at below 5 GHz, we corrected for the dispersive ionospheric delays. Then, we corrected for the parallactic angle and performed global fringe-fitting for the calibrator sources. We imaged the phase-calibrator with the `DIFMAP` software (Shepherd et al. 1994), using the hybrid mapping technique with `CLEAN` deconvolution (Högbom 1974). It included several iterations of cleaning and phase self-calibration before we performed an overall amplitude self-calibration to obtain the antenna-specific gain correction factors. We then applied these amplitude corrections for telescopes with $> 5\%$ deviation from the gain solutions in AIPS. Using the `CLEAN` component (CC) model we built up in `DIFMAP`, we repeated the fringe-fitting in AIPS for the phase-reference calibrator source to correct for the source structure since it contributes to the measured interferometric phases. Finally, we interpolated the solutions of the last fringe-fitting to the data of our target source. As a final step, we exported the calibrated visibility file from AIPS to `DIFMAP` for imaging purposes described in the following.

After flagging the outlier data points, we imaged the target source using the hybrid mapping technique including the `CLEAN` algorithm and phase-only self-calibration. Then, we obtained the antenna-specific gain correction factors. At the end of the procedure, several steps of amplitude and phase self-calibration were performed, starting from the total observation time, gradually for shorter and shorter solution time intervals.

A simple elliptical Gaussian model component (Pearson 1995) was fitted directly to the visibility data. This way we can describe the brightness distribution of the radio source for a quantitative analysis and to reveal any possible structure of it. Finally, to decrease the noise level, we performed 1000 `CLEAN` iterations in the residual image with a small loop gain of 0.01.

3.4.2. ATCA monitoring

The Australia Telescope Compact Array (ATCA)⁵, located at Narrabri, New South Wales, Australia, was used to monitor AT2019aalc. The observations were conducted between 2023-06-28 and 2024-05-04, utilizing the array in the 6km (6A and 6D) and (H168) configuration. The observations were conducted at frequencies of 2.1 GHz, 5.5 GHz, 9 GHz, 17 GHz and 19 GHz. The flux calibrator was the standard ATCA primary calibrator,

⁴ Wb, T6, Ur and the e-MERLIN (Cm, Da, De, Kn, Pi) antennas had no or bad system temperature measurements, we used nominal values for amplitude calibration.

⁵ <https://csiropedia.csiro.au/australia-telescope-compact-array/>

1934–638, and 1548+056 is used as phase calibrator. The observations are summarized in Table 1.

The data reduction procedures were based on the Multi-channel Image Reconstruction, Imaging Analysis and Display (*miriad*; Sault et al. 1995). The data reduction procedure was conducted in accordance with standard protocol. In order to mitigate the impact of radio frequency interference (RFI) during flux and phase calibration, the interactive flagging tool *bflag* was utilised. Furthermore, automated flagging routines *pgflag* were applied to address interference for the source. Any corrupted data identified during calibration was manually flagged.

Due to the limited (u, v)-coverage and the low elevation of the source resulting in a very elongated beamshape, we were not able to perform self-calibration and cleaning. Fortunately, AT2019aalc was always dominating the flux within the resolution elements of our short observations. Therefore, we imaged the region around our source for each observation using an over-sampling of the synthesised beam by a factor of at least 10. Under the assumption that AT2019aalc is always a point-source, we can take the highest pixel value in the image as our measured flux. Due to the uncertainties this method introduced we used a plain 10 % flux error.

3.5. Spectroscopic observations

The Low Resolution Imaging Spectrograph (LRIS; Oke et al. 1995) mounted on the Keck-I telescope at Maunakea measured the spectrum of AT2019aalc, on 2021-07-06 (PI: Kulkarni), almost exactly at half time between the two optical flares. At that time the source was not significantly detected with ZTF as indicated by the forced photometry results. Later, during the second optical flare, we obtained 5 more optical spectra of AT2019aalc using the following instruments: LRIS (PI: Kulkarni), DeVeny Spectrograph mounted on the Lowell Discovery Telescope (LDT) in Arizona (PI: Hammerstein) and the Double Beam Spectrograph (DBSP, Oke & Gunn 1982) mounted on the 200 inch telescope at Palomar Observatory, California (PIs: Kulkarni and Kasliwal). These optical spectra were reduced following the standard procedures using the automated reduction pipeline of the LRIS (Perley 2019), the software package *PYPFIT* (Prochaska et al. 2020) for DeVeny, and the software packages DBSP DRT (Mandigo-Stoba et al. 2022) and *PYPFIT* (Prochaska et al. 2020) for the DBSP. We normalized the flux of each spectrum and plotted it versus the rest-frame wavelength. Details of these observations of AT2019aalc are summarized in Table 2. The obtained spectra cover a timescale of a year and allow us to study the spectroscopic evolution of the transient during its optical re-brightening. We describe the features of each spectra in Subsect. 4.5 and discuss the remarkable lines in Subsect. 5.1.

To determine the type of AGN, we performed a stellar population synthesis fit of the host galaxy’s SDSS spectrum with (*pPXF*; Cappellari & Emsellem 2004; Cappellari 2017, 2023) and the newest GALAXEV (Bruzual & Charlot 2003) models (CB2019), assuming a Kroupa (2001) initial mass function (IMF) and an upper mass limit of 100, as templates. Beforehand, the spectrum was corrected for Milky Way extinction using the dust reddening maps by Schlafly & Finkbeiner (2011) and Cardelli et al. (1989) extinction curve. Furthermore, it was redshift corrected and logarithmically rebinned. We included several emission lines to the fit and assumed four kinematic components: One for all stellar templates, one for all forbidden lines, one for all allowed emission lines, and a last one for a second, broad component of all Balmer lines up to H δ . Additionally, we included two separate dust components, each one with the

extinction curve of Cardelli et al. (1989): a first one for stellar, and a second one for nebular emission. We therefore fixed the Balmer line ratio and limited doublets of the preinstalled lines to their theoretical ratio using the keywords *TIE_BALMER* and *LIMIT_DOUBLETS* of *pPXF*. However, we only fixed the ratio for the strongest lines of the Balmer series up to H δ to avoid possible contamination of H ϵ by the [Ne III] λ 3967 line. For the fit with *pPXF* we included additive and multiplicative polynomials up to tenth order (*DEGREE*=10, *MDEGREE*=10). In order to correct for intrinsic dispersion caused by the spectrograph, we assume a resolving power of 1500 at 3800 Å and 2500 at 9000 Å.⁶ Linear interpolation is used to calculate values for wavelengths in between.

The SPS fit of the latest DBSP spectrum was conducted in a manner analogous to the one applied to the SDSS. However, additional kinematic components were required to account for the internal structure in order to achieve a satisfactory result. Each emission line with an excitation potential above 100 eV is treated as a separate component. The [S II] λ 6731 doublet is fitted as an additional component as well.

4. Results

4.1. Optical/UV

The optical and UV light curves of AT2019aalc are shown in the bottom panel of Fig. 5. The transient was first detected by the ZTF in January 2019 with a *g*-band magnitude of 18.44 mag. After the initial detection of the first optical flare in May 2019 ($g \approx 18.1$), AT2019aalc had brighten to a peak magnitude of $r \approx 16.7$ ($M = -19.4$) reached on 2019-06-18 on a timescale of roughly 60 days. After the quickly and monotonically evolving flare, a slow decay has started, and the source was last detected with ZTF on 2021-02-18 with a magnitude of $g \approx 18.3$ before its second flare. The re-brightening started mid-May 2023, approximately 4 years after the initial flare (Veres et al. 2023). The second flare has evolved very similarly to the original one. From the beginning of the second flare (the source was detected anew on 2023-05-11 at $r \approx 19.3$ mag), a 2.8 mag rise can be seen till the peak of the flare on 2023-07-13 with $r \approx 16.2$ mag ($M = -19.8$), on a timescale of only 60 days. Both flares evolved with constant color. However, the second flare peaked at roughly 1.5 times the peak luminosity of the first flare. The peak of the second flare was followed by a short plateau phase lasted for around 25 days. Both flares decay very slowly, on timescales of years. The first flare decayed with a power-law index of $b \approx -0.45$ while the second has been decaying even slower with a power-law index of $b \approx -0.13$ in *r*-band. The decaying phases are not monotonous as bumps are tend to appear.

Prior to the discovery of AT2019aalc, the host galaxy of the transient has been monitored by several optical surveys. To study the optical variability of AT2019aalc prior to the first optical flare in 2019, we performed aperture photometry of the All-Sky Automated Survey for Supernovae (ASAS-SN; Shappee et al. 2014; Kochanek et al. 2017) using ATLAS forced photometry server (Tonry et al. 2018; Smith et al. 2020) and the Catalina Real-Time Transient Survey (CRTS; Djorgovski et al. 2011) data. In addition, Palomar Transient Factory (PTF Law et al. 2009) magnitudes were extracted from the PTF Lightcurve Table⁷. No significant optical variability can be seen between April 2005 and the discovery of the transient in January 2019 by ZTF (see Fig. 4).

⁶ https://www.sdss4.org/dr17/spectro/spectro_basics/

⁷ <https://irsa.ipac.caltech.edu>

Table 1. Summary of the ATCA radio continuum emission observations of AT2019aalc

Date	Exp. time / min	Configuration	Central Freq. / GHz	Bandwidth / GHz	Flux Calibrator	Phase Calibrator
28.06.2023	330 / 180	6D	2.1 / 7.0	1 / 4	1934-638	1548+056
30.06.2023	90 / 180	6D	2.1 / 7.0	1 / 4	1934-638	1548+056
08.07.2023	120 / 120	6D	2.1 / 7.0	1 / 4	1934-638	1548+056
19.07.2023	210	6D	2.1	1	1934-638	1548+056
09.08.2023	120 / 150	6D	2.1 / 7.0	1 / 4	1934-638	1548+056
19.10.2023	180 / 180	H168	2.1 / 7.0	1 / 4	1934-638	1548+056
09.02.2024	60 / 60 / 60	6A	2.1 / 7.0	1 / 4 / 4	1934-638	1548+056
29.03.2024	60 / 60 / 60	6A	2.1 / 7.0 / 17.0	1 / 4 / 4	1934-638	1548+056

Table 2. Summary of the optical spectroscopic observations of AT2019aalc. δt_{f2} is time relative to the optical peak of the second flare.

Date	δt_{f2}	Telescope	Instrument	Exp. time
	(d)			(s)
Post-flare-1				
2021-07-06	-737	Keck-I	LRIS	300
Over-flare-2				
2023-06-15	-21	Keck-I	LRIS	300
2023-06-22	-28	LDT	DeVeny	800
2023-07-11	-2	Palomar Hale 5 m	DBSP	180
2023-08-17	+35	Palomar Hale 5 m	DBSP	900
2024-05-21	+315	Palomar Hale 5 m	DBSP	1200

Both optical flares of AT2019aalc detected by ZTF rising with constant color $g - r \approx 0$ and show reddening when decaying. The second flare has similar color evolution to the first one when evolving but with a color of $g - r \approx 0.2$ around the peak.

The first optical flare was not monitored in UV. The UV monitoring of the source started on 2023-06-23 around 20 days before the optical peak of the second flare. The UV flare evolved quickly. The U-band peak is coincident with the optical peak while the shorter wavelength bands (UM2, UW1 and UW2) peaked 2 – 4 weeks later⁸. The transient is most luminous at the shortest wavelength ranges covered by UVOT. The UV emission peaks around 10^{44} erg/s in filter UW2. After the peak epoch, the UW2–U color shows reddening which suggests increasing absorption or a drop of the blackbody temperature. Towards the end of the UVOT monitoring, the measured UM2 magnitudes decrease back to the level of the baseline GALEX-NUV magnitudes measured between 2007 and 2011.

Comparing the peak UVM2 magnitude of the UVOT monitoring to the GALEX-DR5 (Bianchi et al. 2011) NUV magnitude implies that the UV luminosity increased by a factor of ≈ 7 with respect to the archival flux. The amplitude of this flare is higher than typically seen for AGN. Only 8 out of the 305 AGN presented in the GALEX Time Domain Survey (Gezari et al. 2013) have larger amplitude NUV variability.

4.2. Infrared

We detected AT2019aalc in all of the three bands observed with the WIRC. The observed magnitudes are plotted in the top panel

⁸ We note that right after the r -band peak, a short plateau phase started in optical and the UV emission in the bands UM2, UW1 and UW2 peak during this plateau

of Fig. 5. The host galaxy of AT2019aalc is presented in the 2MASS All-Sky Catalog of Point Sources (Cutri et al. 2003) as 2MASS 15241666+0451191. The observed magnitudes in April 2000 are higher with ≈ 0.5 mag in J-, and Ks-bands and with ≈ 0.6 mag in H-band indicating the clear brightening of the IR counterpart with respect to archival data.

The top panel of Fig. 5 also shows the long-term light curve starting just before the first optical flare. There are clear signs of variability throughout the infrared light curve starting in February 2010 with the distinct first dust echo flare that peaks around six months after the first optical peak. The rise of the dust echo of the second flare becomes visible in the latest WISE data release. The light curve varies by around 0.3 mag in W1 and 0.4 mag in W2 before the dust echo flare, which is consistent with statistical AGN variability (Berk et al. 2004). In contrast, the dust echo presents an increase of 1.0 mag in W1 and 1.2 mag in W2. The first detection of the dust echo of the second flare shows a brightening of 0.8 mag in both bands and can be expected to increase further in upcoming data releases. Because the brightness is significantly above the limiting magnitude where Eddington bias becomes an issue for stacked single-exposure photometry (Necker et al. 2024), we can estimate the pre-flare mid-IR color using the median of the light curve prior to the dust echo flare with $m_{W1} - m_{W2} \approx 0.6$. Although there is clear AGN activity prior to the dust echo flare, this is still below the widely used AGN identification cut of $m_{W1} - m_{W2} \geq 0.8$ (Stern et al. 2012). However, according to the reliability of WISE selection as a function of a simple W1–W2 color selection (Stern et al. 2012), the color of AT2019aalc suggests a reliability of only $\approx 70\%$. With the onset of the dust echo, the IR emission becomes dominated by the heated dust, which is shown in Fig. 6. The change from bluer to redder colors come from cooling of the dust. The re-brightening of the second dust echo is consequently accompanied by another color change towards the blue.

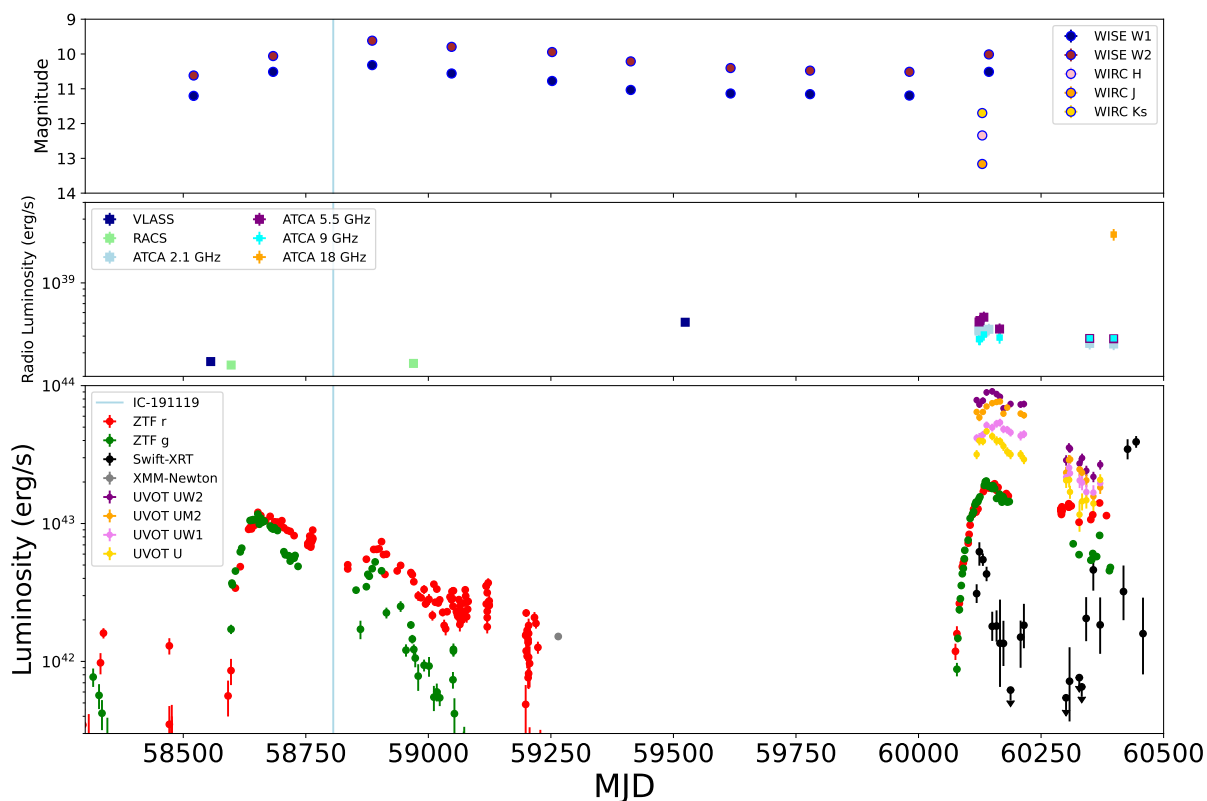


Fig. 3. Multi-wavelength (bottom plot: optical/UV and X-ray, middle plot: radio and upper plot: IR) light curves of AT2019aalc. Here we show only the positive ZTF fluxes based on the forced photometry results. The light blue vertical line indicates the IceCube detection of the high-energy neutrino event IC-191119.

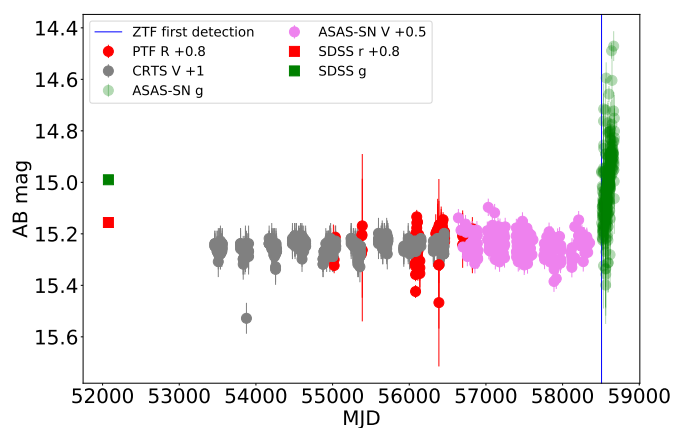


Fig. 4. Long-term optical light curves of the host galaxy of AT2019aalc spacing approximately 14 years before the discovery of the transient in January 2019 indicated with a blue vertical line. No obvious signs of variability can be seen before the first detection of the transient by the ZTF.

Notably, AT2019aalc is not part of the Flaires sample (Necker et al. 2024), a list of dust-echo-like infrared flares interpreted as extreme AGN accretion events or TDEs. This is because the broad application of the Flaires pipeline necessarily

included a strict cut on extraneous variability that AT2019aalc did not pass. The authors did note however that a desirable relaxation of this criterion would include AT2019aalc. The source is, however, part of the dust echo sample of van Velzen et al. (2024) and, notably has the highest dust echo flux of all ZTF transients.

4.3. X-ray

AT2019aalc was monitored with the *Swift*/XRT at 0.3 – 10 keV energies for 11 weeks with weekly cadence around the peak of the optical flare and later for additional months with weekly and bi-weekly cadences. The luminosity evolution is shown in the bottom panel of Fig. 5 while the count rate variability is plotted in the top panel of Fig. 7. The first two visits show an increase of the X-ray emission. This flaring episode peaked at $L_X \approx 6 \times 10^{42}$ erg s⁻¹ on 2023-06-29 (MJD= 60124) (see Fig. 5.) before it experienced a very quick decreasing. This flare peaked 2 weeks before the optical peak. The count rate dropped by a factor of ≈ 10 , from 0.05 to 0.005, within a timescale of ≈ 60 days. Later, the X-ray emission shows limited variability for several months, however, less significant flaring episodes appear that peaked in the end of September 2023 (MJD= 60215) and mid-February 2024 (MJD= 60356). The latter was followed by a bump in the optical and UV light curves around 2 weeks later while no optical/UV data is available around the another X-ray increasing. In the end of April 2024, a rapid and extreme flaring episode was

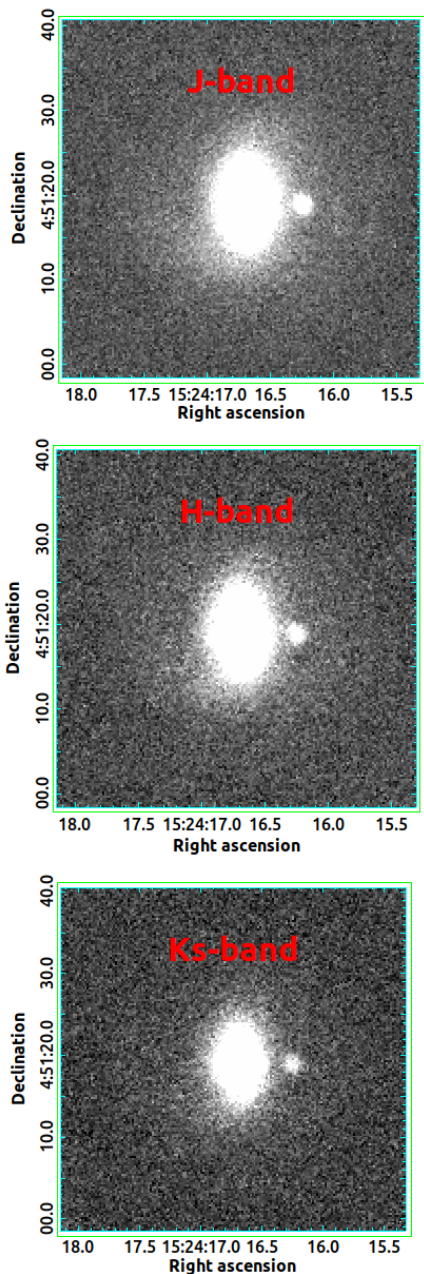


Fig. 5. The WIRC infrared images of AT2019aalc in J-, H-, and Ks-bands taken on 2023-07-05 (roughly a week before the optical peak). The object located to the west from the target source is a foreground star.

detected in X-rays that lasted less than a month but reached a luminosity of $L_X \approx 4 \times 10^{43}$ erg/s which is almost a magnitude larger compared to the peak of the first X-ray flaring episode. Interestingly, this X-ray flare was also accompanied by an increasing phase in the optical 1 – 2 weeks later, according to the most recent ZTF observations⁹. Notably, ≈ 90 days passed between both the first and second and the third and fourth X-ray flaring episodes. While no data is available for a longer period between the second and third flares when the source was too close to the Sun.

In Fig. 8 we show the source spectrum derived from the full observing campaign. The spectrum is dominated by a power-law

⁹ <https://lasair-ztf.lsst.ac.uk/objects/ZTF19aaejtoy/>

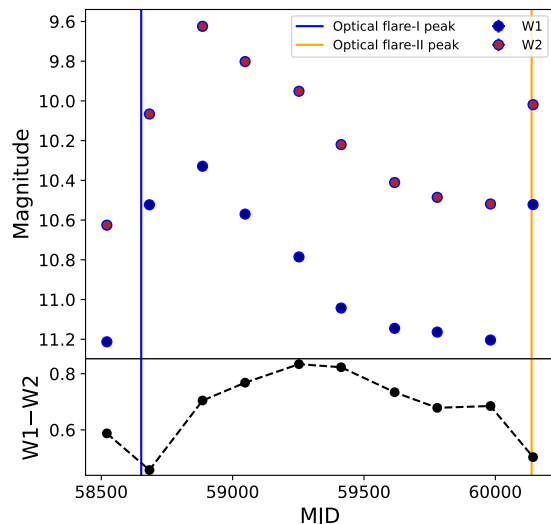


Fig. 6. The long-term IR variability of AT2019aalc based on WISE magnitudes in W1 and W2. The W1–W2 color indicates heated dust as the dominant origin of the IR emission. The second optical flare seems to be accompanied by another IR flaring episode with color change towards the blue.

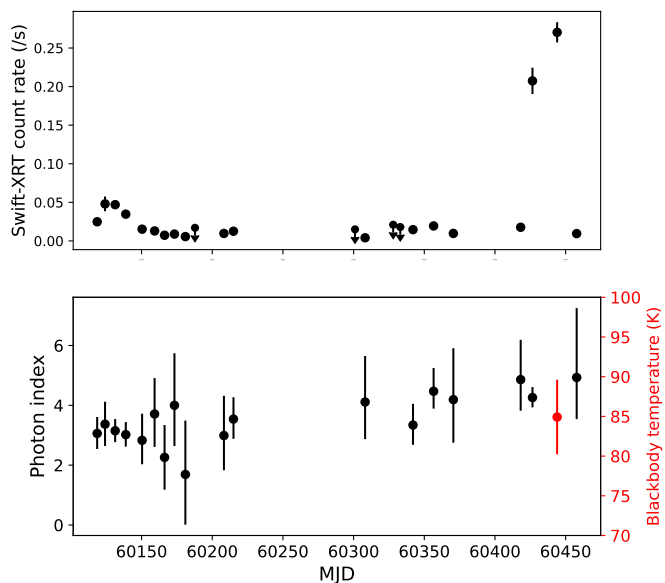


Fig. 7. The Swift-XRT count rate and photon index variability of AT2019aalc during the observing campaign. In most cases the data is well described by a power-law spectral model (black), except during the most recent flaring episode, where a blackbody model is preferred (red). The blackbody temperature is indicated on the red y-axis.

component but a blackbody component is also significantly presented. The spectral index of the stacked spectrum fitted with a power-law+blackbody model is $\Gamma = 2.8^{+0.4}_{-0.4}$ while the blackbody temperature is $kT = 89^{+10}_{-12}$ eV. These imply an overall unabsorbed flux of $F_X = 5.1^{+0.15}_{-0.15} \times 10^{-13}$ erg cm⁻²s⁻¹ corresponding to a luminosity value of $L_X = 1.55^{+0.15}_{-0.14} \times 10^{42}$ erg/s. The count

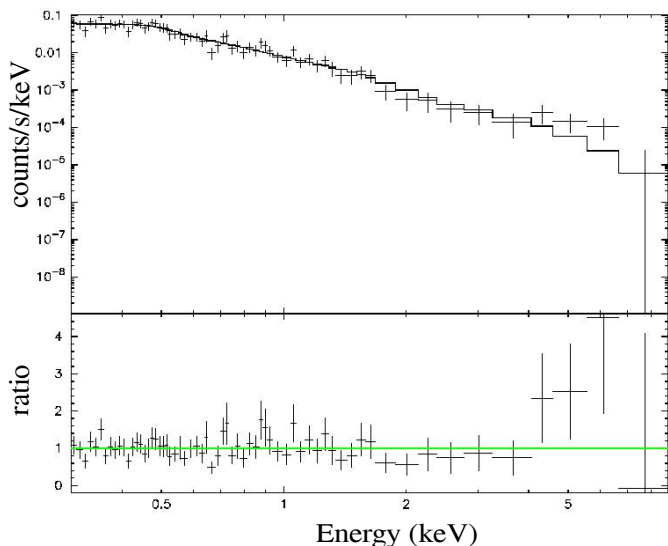


Fig. 8. The overall *Swift*-XRT 0.3 – 10 keV spectrum of AT2019aalc. We binned the spectrum to have a minimum of 5 counts per spectral bin and fit with an absorbed blackbody+power-law model.

rate of the observations is 0.028 ± 0.001 cts s^{-1} . The photon index variability of AT2019aalc is presented in the bottom panel of Fig. 7.

AT2019aalc (= SRGe J152416.7+045118) was observed by the eROSITA (Sunyaev et al. 2021) soft X-ray telescope four times starting from 2020-02-02 (roughly half year after the peak of the first optical flare) with a 6 months cadence. The X-ray light curve reached a plateau between August 2020 and January 2021 with a flux of $F_X \approx 4.6 \times 10^{-13}$ erg $cm^{-2}s^{-1}$ in the energy range of 0.3 – 2 keV. The source had a soft thermal spectrum described with a blackbody temperature of $kT = 172 \pm 10$ eV (van Velzen et al. 2024). One observation with XMM-Newton Observatory (Jansen et al. 2001) has been performed in 2021-02-21 during a period of optical quiescence. The best-fit power-law index and the observed 0.3 – 8 keV flux of this observation were $\Gamma = 2.6^{+0.1}_{-0.1}$ and $F_X \approx 5.1^{+0.15}_{-0.25} \times 10^{-13}$ erg $cm^{-2}s^{-1}$ (68% confidence), respectively (Pasham 2023). These imply that the two X-ray flares observed with the *Swift*/XRT peaked at much higher luminosities than the plateau or long-term flaring episode between the optical flares, however, there is no X-ray data from around the peak of the first optical flare. Furthermore, the eROSITA results confirm the presence of a blackbody component in the X-ray spectrum, which is very soft and dominating the variability of the X-ray source.

4.4. Radio

4.4.1. Temporal evolution

The host galaxy of AT2019aalc was detected in the NRAO VLA Sky Survey (NVSS, White et al. 1997) in February 1995 and in the FIRST survey in February 2000 (both at 1.4 GHz) with peak flux densities of 6.0 ± 0.5 mJy and 6.2 ± 0.1 mJy respectively, suggesting no substantial variability of the host galaxy prior to the discovery of the transient event.

Later, the transient’s sky location has been observed during the first and second epochs of the Very Large Array Sky Survey (VLASS). The VLASS covers the entire sky visible to the Karl G. Jansky Very Large Array (VLA) at 2 – 4 GHz wide

band offering an angular resolution of 2.5 arcsec and an rms of 0.12 mJy $beam^{-1}$ in each epoch (Lacy et al. 2020). One of the main goals of the VLASS multi-epoch survey is to detect various types of extragalactic radio transients, such as TDEs, accretion state changing AGNs and core-collapse supernova (Lacy et al. 2020; Zhang et al. 2022). To date, the first two epochs of the survey have been fully published. Our source has peak flux density values of 2.9 ± 0.2 mJy/beam (on 2019-03-14) and 5.7 ± 0.2 mJy/beam (on 2021-11-06), corresponding to 3 GHz radio luminosities of 3×10^{38} and 5×10^{38} erg s^{-1} in the Epoch 1 and Epoch 2 images, respectively. This factor of ≈ 2 increase in flux from the first VLASS epoch (three months before the optical peak) to the second VLASS epoch (2 years post-peak) is statistically significant (at the 8σ -level, as estimated from the rms in the VLASS “Quick Look” images, van Velzen et al. 2024).

In addition, we found a radio source at the position of AT2019aalc in the first data release (DR1) of the Rapid ASKAP Continuum Survey (RACS; McConnell et al. 2020). The RACS DR1 includes initial observations made for RACS-low (central frequency of 888 MHz)¹⁰. Moreover, the source has been observed in two different fields and, consequently, at two different epochs. The observed peak flux densities of 9.2 ± 0.5 mJy/beam (on 2019-04-24) and 9.5 ± 0.5 mJy/beam (on 2020-04-30) correspond to a 888 MHz radio luminosity of $\approx 2.5 \times 10^{38}$ erg s^{-1} and indicate that the radio flare seen in the VLASS data started at least 300 days after the peak of the first optical flare, sometime between April 2020 and November 2021.

Interestingly, the radio luminosity in the beginning of our ATCA monitoring is at the same level within uncertainties ($L_R \approx 5 \times 10^{38}$ erg s^{-1}) when the source was observed for the second time in the VLASS in April 2021. Since the radio brightness does not show rapid variability during the months of our ATCA monitoring, we can reasonably assume that the sharp increasing resulted in a long-lasting plateau. Our multi-frequency monitoring with the ATCA implies no substantial variability on monthly timescales at 9 GHz while it shows slow decreasing at 2.1 GHz and at 5.5 GHz over time. We observed the radio source at 17 – 19 GHz at one epoch. We present the ATCA radio multi-frequency light curves of AT2019aalc together with the archival observations in the middle panel of Fig. 5 and focusing on the ATCA monitoring in Fig. 9.

4.4.2. The radio spectrum

To further characterize the radio emission of AT2019aalc, we derived the radio spectral index of the radio source in each epoch of our ATCA monitoring. The spectral index between 2.1 GHz and 9.0 GHz (α , defined as $S \propto \nu^\alpha$) does not show any obvious signs of variability on a timescale of 9 months. We give an average spectral index of $\alpha_{2.1GHz}^{9GHz} \approx -1.1$. We calculated a pre-flare spectral index using the VLASS epoch 1 and RACS epoch 1 flux densities (these flux values are explained in Sect. 4.4.1.). The spectral index we derived between 0.888 GHz and 3.0 GHz this way is $\alpha_{888MHz}^{3GHz} = -0.96 \pm 0.07$.

Our high-frequency K-band observations centered at 18 GHz, however, do not follow the steep power-law and suggest a turnover between 9 GHz and 18 GHz. The spectrum of high frequency peaked radio sources are usually explained with significant absorption taken place in the system due to synchrotron self-absorption (although free-free absorption may also play a

¹⁰ <https://www.cadc-ccda.hia-ihp.nrc-cnrc.gc.ca/en/racs/>

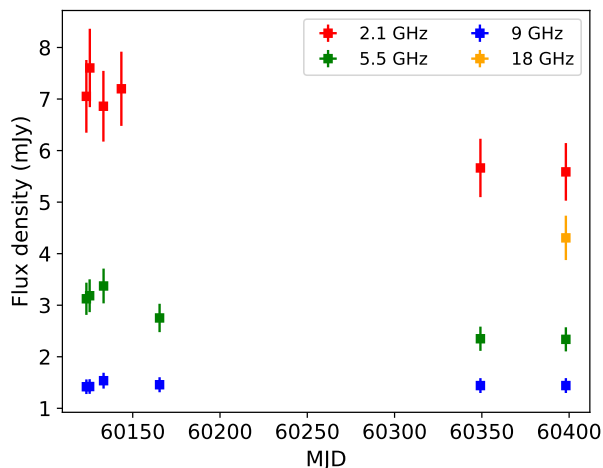


Fig. 9. The radio flux density evolution of AT2019aalc during the time interval of our ATCA monitoring of the transient at 4 different frequencies.

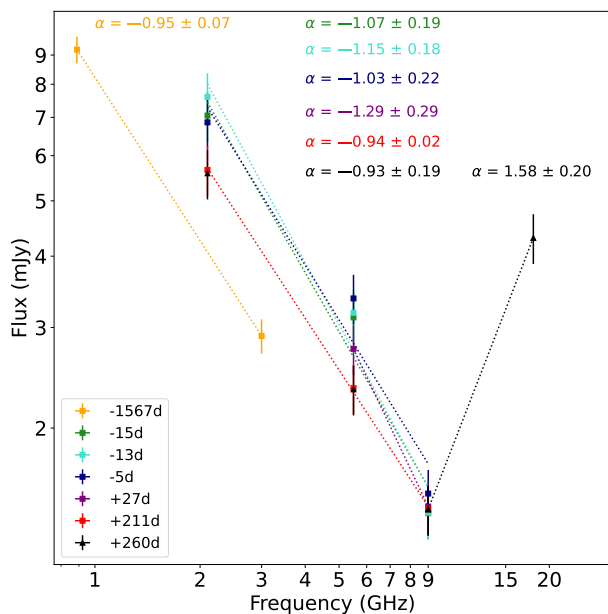


Fig. 10. Radio spectra of AT2019aalc between 3 GHz and 18 GHz based on our ATCA monitoring. We derived a prior radio flare spectrum between 888 MHz and 3 GHz from archival fluxes. The times in the legend are relative to the peak of the second optical flare.

role, (e.g., [Berton et al. 2020](#)). We further discuss the features of the radio spectrum in [Subsect. 5.3](#).

4.4.3. VLBI detection

The final naturally-weighted VLBI map of AT2019aalc is shown in [Fig. 11](#). We detected a single radio-emitting feature with a signal-to-noise ratio (SNR) of $\approx 19\sigma$ with our 1.7 GHz EVN+e-MERLIN VLBI observation. We obtained the following parameters of the fitted component; a total flux density of $S = 21.0 \pm 1.8$ mJy and a size of $d = 2.23 \times 1.39 \pm 0.3 \times 0.3$ mas at a position

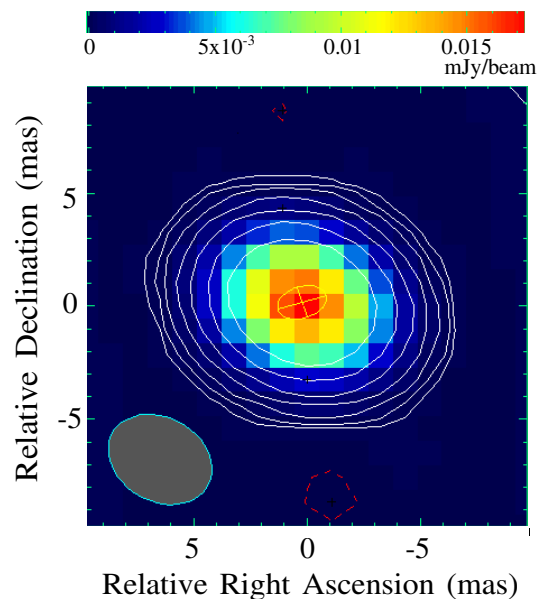


Fig. 11. Naturally weighted 1.7 GHz EVN+e-MERLIN high-resolution VLBI map of AT2019aalc. The peak brightness is 17.3 mJy beam $^{-1}$. The grey ellipse in the lower-left corner represents the Gaussian restoring beam. Its parameters are 4.82 mas \times 3.7 mas (FWHM) at a major axis position angle of $PA = 60^\circ 8'$. The lowest contour level is drawn at $\pm 3\sigma$ image noise level corresponding to 0.08 mJy beam $^{-1}$. Further positive contour levels increase by a factor of 2. The red dashed contours represent the negative contours. The yellow ellipse is the fitted Gaussian model component to describe the brightness distribution of the radio source.

angle of $\phi = -73.3^\circ$. We calculated the uncertainties of the flux density and size parameters following the formulas of [Fomalont \(1999\)](#). The minimum resolvable size (θ_{lim}) of a Gaussian component fitted to naturally weighted VLBI data was calculated following [Kovalev et al. \(2005\)](#). This yields $\theta_{\text{lim}} = 1.05 \times 0.81$ mas implying that the fitted Gaussian component is resolved. We note that at high SNR, θ_{lim} can be significantly smaller than the size of the resolving beam ([Bertero & de Mol 1996](#); [Kovalev et al. 2005](#)) due to applying a specific a priori hypothesis about the shape of the emitting region which is in our case the two-dimensional Gaussian used to fit the observed brightness distribution of the radio source.

The positional uncertainty was estimated as follows. When calculating the VLBI positional uncertainty, we took into account both the positional uncertainty of the phase calibrator source and its angular separation from our target source. The position of the phase calibrator source is listed with an error of 0.18 mas in the third realization of the International Celestial Reference Frame (ICRF3; [Charlot et al. 2020](#)). The angular separation between the target and the calibrator source signifies a positional error of about 1.5 mas at 1.7 GHz ([Chatterjee et al. 2004](#)). The resolution of the observation depending on the thermal noise of the interferometric images ([Reid et al. 1988](#)) has been also considered. Following [Reid et al. \(1988\)](#), we estimated a thermal noise-limited positional accuracy of 0.1 mas. The resultant positional uncertainty of 1.5 mas is therefore dominated by the uncertainty arising from the angular separation between the calibrator and the target source. The radio position agrees with the source position in the *Gaia* DR3 ([Gaia Collaboration et al. 2023](#)) catalog within the positional uncertainties.

We calculated the brightness temperature of the radio-emitting feature found at the position of AT2019aalc using the following equation (Condon et al. 1982; Ulvestad et al. 2005):

$$T_b = 1.22 \times 10^{12} (1+z) \frac{S}{\theta_{\text{maj}} \times \theta_{\text{min}} \nu^2} \text{ K}, \quad (1)$$

where S is the flux density of the fitted Gaussian component measured in Jy, θ_{maj} and θ_{min} are the major and minor axes full width at half maximum (FWHM) of the fitted component in mas, and ν is the observing frequency in GHz. The obtained brightness temperature is $T_b = (3.0 \pm 0.8) \times 10^9$ K at 1.7 GHz. The brightness temperature is an effective parameter that is commonly used in radio astronomy to describe the physical properties of emitting material in astrophysical objects (e.g., Lobanov 2015). It can be determined by imaging and modeling the structure of a given emitting region. The derived value is crucial to characterize the detected radio emission, which can be either thermal or non-thermal.

4.5. Spectroscopic results

We present the archival and the newly obtained optical spectra of AT2019aalc in Fig. 12 with marking the notable emission lines. In the following, we highlight the remarkable line detection of the host spectrum observed before the first optical flare (pre-flare spectrum), the one observed between the two flares (post-flare-1 spectrum) and 5 spectra that were taken during the second flare (over-flare-2 spectra).

4.5.1. Pre-flare spectrum

A spectrum of the host galaxy of AT2019aalc was taken in April 2008 by the SDSS spectrograph. We present this spectrum with the best fits for the stellar and gas components in Fig. 13.

- We identify strong Balmer emission lines. These lines are generally thought to be originating from the broad-line region i.e. the vicinity of the SMBH. We estimate the FWHM of the Balmer lines to $\text{FWHM}(\text{Balmer}) \approx 2800 \text{ km s}^{-1}$ for the broad component of the Balmer lines (see Fig. 13 subplots) in the host spectrum, which is typical for an unobscured, broad line AGN. The line widths ($\text{FWHM}(\text{Balmer}) \approx 2600 \text{ km s}^{-1}$) presented in the SDSS DR7 broad-line AGN catalog (Liu et al. 2019) for our source are consistent with this classification. In addition to the Balmer lines, we detect the recombination line $\text{He I } \lambda 5876$ which is also produced in the BLR.
- The remarkable $[\text{O III}] \lambda 4959$ and $[\text{O III}] \lambda 5007$ forbidden lines exhibited already in the SDSS spectrum indicate that the host AGN was not completely dormant before the optical flares, which is further supported by the radio detections prior to the first flare (Subsect. 4.4.1). Other forbidden emission lines commonly seen in AGN such as $[\text{S II}] \lambda 6716$, $[\text{S II}] \lambda 6731$ and $[\text{N II}] \lambda 6584$ are detected as well. These lines are produced in the narrow-line region (NLR) in AGN. We note that the sulfur lines are also present in the spectra of the TDE AT2019dsg, which was hosted by a quiescent galaxy. We detect the $[\text{O II}] \lambda 3726$ + $[\text{O II}] \lambda 3729$ line doublet, which is a potential indicator of star formation or AGN-driven outflows (e.g., Santoro et al. 2020).

4.5.2. Post-flare-1 spectrum

The first LRIS spectrum was taken almost 2 years after the first flare and 2 years before the second one.

- We detected an increase in the Balmer lines series and the forbidden lines $[\text{O III}] \lambda 4959$ and $[\text{O III}] \lambda 5007$. The Balmer lines are also remarkably broadened.
- In addition to the strong Balmer emission lines, we can identify the $\text{He II } \lambda 3203$ He II and $\lambda 4686$ transitions and the Bowen Fluorescence line $\text{O III } \lambda 3133$. Wavelength coincidences between emission lines ("line fluorescence") can be an important source of radiative excitation. In the case of Bowen Fluorescence, the He II-O III and N III coincidences lead the mechanism. The BF lines occur due to the excitation in certain states of O III and N III by the absorption of $\text{He II Lyman } \alpha$ photons. These excited states lead to a cascade of transitions that can be observed as emission lines in the optical and NUV regimes (Netzer 1990; Trakhtenbrot et al. 2019). Interestingly, the existence of BF emission lines in astronomical objects has been predicted by Netzer et al. (1985) as the required gas densities are consistent with what is expected from the extremely dense environment in some AGN and gaseous nebulae.
- We detect the high ionization coronal lines $[\text{Fe VII}] \lambda 6089$, $[\text{Fe X}] \lambda 6375$ and $[\text{Fe XIV}] \lambda 5303$. The very high ionization potentials of 235 eV and 262 eV of $[\text{Fe XIV}] \lambda 5303$ and $[\text{Fe X}] \lambda 6375$, respectively, point to very energetic processes at work. First Oke & Sargent (1968) studied coronal lines in detail in a Seyfert galaxy (NGC 4151). These lines are commonly detected in AGN and commonly thought to be powered by photoionization of the NLR (Cerqueira-Campos et al. 2021). In some extreme cases, a shock model i.e. collisional ionization for the coronal line region is required to explain the origin of these lines as it is the case in the Seyfert galaxy NGC 1068 (Oliva 1997).
- We identify the $[\text{Ne V}]$ emission lines at 3345 \AA and 3426 \AA in the spectrum. These lines are not strongly excited in the inner regions of AGNs, but are prominent emission lines in the lower density extended emission line regions (EELRs) excited by the AGN via photoionization or shocks. The forbidden line $[\text{O III}] \lambda 4363 \text{ \AA}$ also appears, however, bending from $\text{H}\gamma$ is possible.

4.5.3. Over-flare-2 spectra

We performed 5 optical spectroscopic observations of AT2019aalc during its second flare. These are characterized by a blue continuum with several lines appearing in comparison to the spectra discussed above. We compare the second LRIS spectrum of AT2019aalc (covering the broadest wavelength range) with a composite SDSS spectrum based on 10112 Seyfert 1 galaxies published in Pol & Wadadekar (2017). This comparison shows similarities but also significant differences discussed below.

- The line widths and strengths of the earlier detected broad Balmer emission lines ($\text{H}\alpha$, $\text{H}\beta$ and $\text{H}\gamma$) increased and both the line widths and strengths of the Balmer lines peaked 2 days before the optical peak. Two lines of the series ($\text{H}\delta$ and $\text{H}\eta$) were detected only in the over-flare-2 spectra.
- Over the second optical flare of AT2019aalc we detected another BF line $\text{N III } \lambda 4640$ together with the transition line $\text{He II } \lambda 4686$. This doublet has not been detected in the

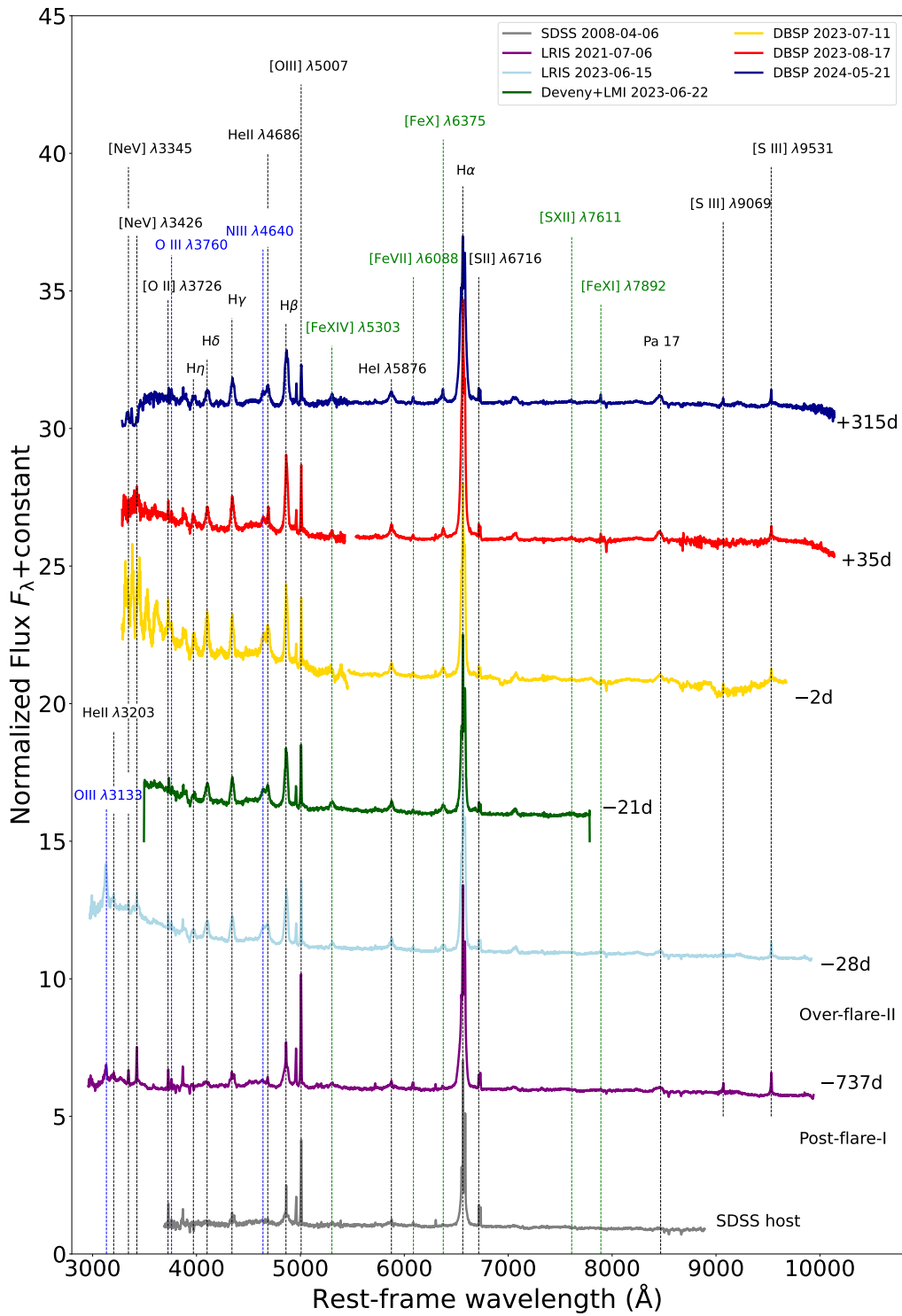


Fig. 12. The optical spectra of AT2019aal normalized between 7400 and 7500 Å. The most remarkable lines are indicated with vertical lines. Days relative to the second optical peak are given to the right from each spectra. The SDSS host spectrum was observed around 11 years before the first optical flare.

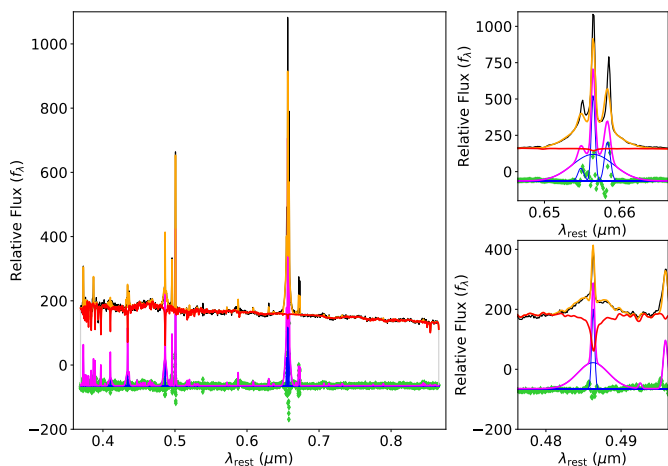


Fig. 13. The SDSS spectrum of the host galaxy of AT2019aalc provided by pPXF supplemented by two subplots showing H α (top right corner) and H β (lower right corner). The input spectrum is shown as solid black line, the best stellar and stellar + gas fit are represented as solid red and orange lines, respectively (Cappellari 2023). Additionally, plotted with an arbitrarily chosen offset, one can see the individual gas components (solid blue), total gas emission (solid magenta) and fit residuals (green diamonds) (Cappellari 2023).

archival SDSS spectrum taken ≈ 11 years before the discovery of the transient or in the post-flare-I spectrum. We detected this doublet already in the first spectrum taken during the second flare. The strengths of these lines increased significantly around the second optical flare and peaked on 2023-07-11, very close to the optical continuum peak (2023-07-13). As we detected the Bowen line N III $\lambda 4640$ even 315 days after the optical peak of the second flare, we can conclude the long-term persistence of at least one BF line after the second flare as well. In addition, the second LRIS spectrum shows a clear increase in the BF line O III $\lambda 3133$ and in He II $\lambda 3203$ when comparing it to the post-flare-1 spectrum. Both lines increased by a factor of ≈ 2 with respect to the post-flare-1 LRIS spectrum. We might detect O III $\lambda 3760$ which is also known as a Bowen line (Selvelli et al. 2007), however, due to a possible blending from Fe VII $\lambda 3759$, its detection is questionable. Nevertheless, this Bowen line is created through the same channel (O1) as the above discussed O III $\lambda 3133$ which suggests its detection. O III $\lambda 3760$ was detected in some metal-rich TDEs before (Leloudas et al. 2019) such as AT2019dsg (Cannizzaro et al. 2021).

- We detect the high-ionization coronal lines seen in the post-flare-1 LRIS spectrum over the second flare in each spectrum. Furthermore, a new coronal line (Fe XI $\lambda 7892$, ionization potential: 361 eV) appears on 2023-08-17, around a month after the peak of the second optical flare. Interestingly, the line intensities of these lines are larger after the optical peak than around the peak in contrast with the BF lines and the above-mentioned ionized helium lines which experienced their maximums very close to the continuum peak. Moreover, [Fe XI] $\lambda 7892$ and [Fe X] $\lambda 6375$ are not just persistent but the strongest in the late-time DBSP spectrum, taken almost a year after the optical peak of the second flare. We detect the high-ionization coronal line [S XII] $\lambda 7611$ only in the late-time spectrum. This line is an extreme ionization line with an ionization potential of 504.8 eV thus implies that unusually high level of ionization is taken place in AT2019aalc

almost a year after its second optical peak. For this coronal line we estimate $\text{FWHM}(\text{S XII } \lambda 7611) \approx 3400 \text{ km s}^{-1}$.

- We detected the [Ne V] emission lines at 3345 Å and 3426 Å in the second LRIS spectrum, similarly to the post-flare-1 spectrum and implying continuous ionization of the EELR. The [O III] $\lambda 4363$ Å line appears in the late-time spectrum.

5. Discussion

5.1. Spectroscopic properties

5.1.1. Balmer lines

The line width of the Balmer lines and its limited variability are not common for regular TDEs and flaring AGN which tend to have decreasing and increasing Balmer line widths over time, respectively (Gezari 2021). However, this behavior is more compatible with the spectroscopic properties of the TDE-AGN PS16dtm (Blanchard et al. 2017). Still, the slight increasing and broadening indicate high-velocity gas moving in the BLR, close to the SMBH. In addition, a more complex structure of these lines seen in the late-time DBSP spectrum.

5.1.2. Bowen lines

The Bowen Fluorescence mechanism in astrophysical environments is a good indicator of absorbed EUV–soft X-ray flux (at wavelengths shorter than the He II Lyman limit of $h\nu \geq 54.4 \text{ eV}$) as these high-energy photons are converted into the He II Lyman α $\lambda 303.782 \text{ \AA}$ emission required for the excitation of the O III and N III (Selvelli et al. 2007). This is consistent with the multiple soft X-ray flares and the extreme UV luminosities of AT2019aalc. The BF line O III $\lambda 3133$ has been observed in the Bowen Fluorescence Flares AT2017bgt (Trakhtenbrot et al. 2019) and AT2021loi and only in a few Seyfert galaxies before (e.g., Malkan 1986; Schachter et al. 1990), however, we note that due to the atmospheric limit at $\approx 3100 \text{ \AA}$ these lines are not easy to detect. This line is typically much weaker in normal Seyfert galaxies as in TDEs, BFFs or in our case (see Fig. 14). The BF line N III $\lambda 4640$ is not generally seen in AGN (e.g., Vanden Berk et al. 2001), however, has been observed in several optical TDEs (Charalampopoulos et al. 2022b) and other SMBH-related transients; the BFFs AT2017bgt, F01004-2237 and OGLE17aaj (Trakhtenbrot et al. 2019) and AT2021loi (Makrygianni et al. 2023), the peculiar transient event AT2019avd (Malyali et al. 2021) and a few flaring NLSy1s (Frederick et al. 2021). In a TDE case, the disrupted star’s material forms an accretion disk and the photosphere absorbs the EUV–soft X-ray photons originating from accretion processes and this way provide a plausible explanation for the appearance of the BF lines. BFFs have been first identified by Trakhtenbrot et al. (2019) who revealed three flares (AT2017bgt, F01004-2237 and OGLE17aaj) in AGN with the appearance of persistent Bowen lines. Later, Makrygianni et al. (2023) studied a transient, AT2021loi, classified as a BFF. The detection of a BF line almost 2 years after the first optical flare of AT2019aalc suggests its long persistence, similar to the cases of the BFFs studied by Trakhtenbrot et al. (2019). In the case of AT2017bgt, this Bowen line was still detected 470 days after the discovery of the transient. These lines in BFFs identified by Trakhtenbrot et al. (2019) may originate from a pre-existing BLR (a region with dense line-emitting gas) which was suddenly exposed to the intense ionizing UV emission, which also indicates enhanced accretion onto the SMBH. Alternatively, the BF lines might be related to

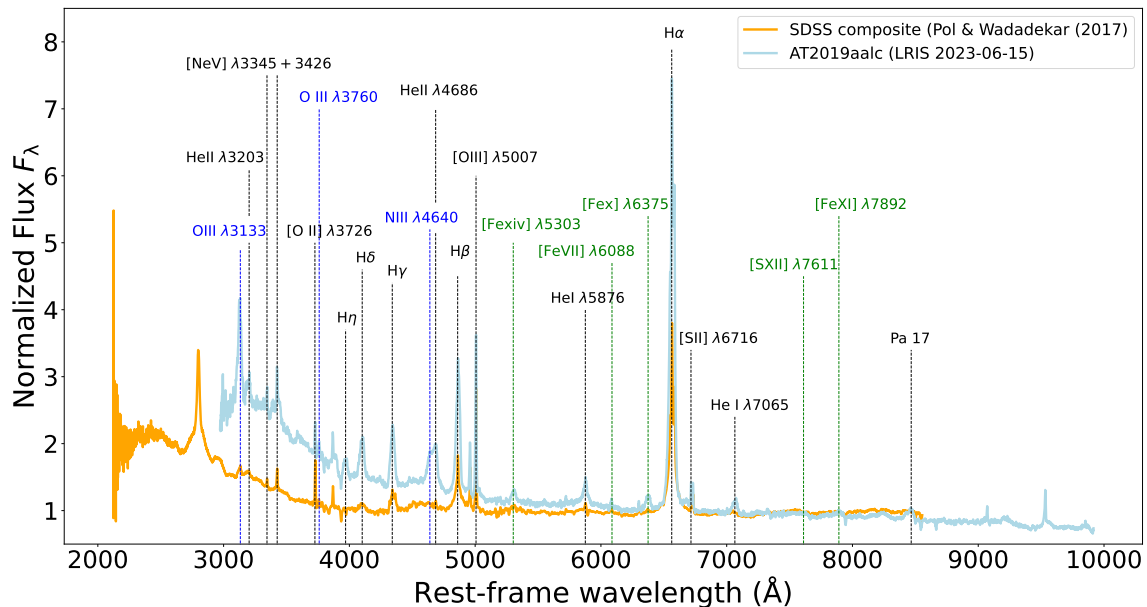


Fig. 14. The over-flare-2 LRIS spectrum of AT2019aalc in comparison with the SDSS composite spectrum of 10112 Seyfert 1 galaxies published in Pol & Wadadekar (2017) and normalized between 7400 and 7500 Å. The most remarkable lines are shown with vertical lines. The most significant differences are the appearance of the Bowen lines (marked with blue) and the high-ionization coronal lines (marked with green) in the spectrum of AT2019aalc and the line strengths of the Balmer line series and the helium lines.

a newly launched outflow driven by a sudden increase in accretion rate which interacts with the BLR. We compare the over-flare-2 high-resolution LRIS spectrum of AT2019aalc with the spectra of the BFFs AT2017bgt and AT2021loi, the BFF candidate AT2019avd, the TDE-Bowen AT2018dyb and the repeating partial TDE AT2020vdq in Fig. 15 with focusing on the N III $\lambda 4640$ +He II $\lambda 4686$ emission line doublet. We further compare the second LRIS spectrum of AT2019aalc with the LRIS spectrum of AT2021loi in Fig. 16 zooming into the O III $\lambda 3133$ and He II $\lambda 3203$ region.

The increasing of these lines around the optical peak indicate that these lines were enhanced by the Bowen Fluorescence mechanism. The BF process is particularly strong in some He II, O III and N III transitions. These lines are obviously detected during the second optical flare, while atypical for normal Seyfert 1 galaxies (see a comparison plot in Fig. 14). Moreover, the O III lines at 3341, 3429 and 3444 Å normally detected in AGN do not show up in our spectra, similarly to the case of AT2017bgt. These results suggest that the BF mechanism plays an important role and this mechanism traces significantly enhanced accretion onto the SMBH suggesting the unusual nuclear transient nature of AT2019aalc.

The He II $\lambda 4686$ ionized helium line is presented in our spectra taken between the optical flares, and is also increased during the second optical flare. This emission line is commonly present in AGN and known as a recombination line, tracing ionized gas in the vicinity of the central SMBH responsible for the photoionization (e.g. Wang & Kron 2020). This line is known to be created by photoionization due to (soft) X-ray photons with a rough correspondence of 1 He II photon emitted for each 0.3 – 10 keV X-ray photon (Pakull & Angebault 1986; Schaerer et al. 2019; Cannizzaro et al. 2021). In the spectra of AT2019aalc, He II $\lambda 4686$ is present together with strong N III and O III BF lines and the less commonly detected He II $\lambda 3203$ tran-

sition, indicating its relation to the Bowen Fluorescence mechanism. Furthermore, we calculated a maximum line intensity ratio of $F(\text{He II})/F(\text{H}\beta) \approx 0.7$ whose value significantly exceeds the typical ratios estimated for AGN (earlier Vanden Berk et al. (2001) estimated ratios of $F(\text{He II})/F(\text{H}\beta) \leq 0.05$ while Shirazi & Brinchmann (2012) gives $F(\text{He II})/F(\text{H}\beta) \leq 0.1$). Our value is, however, more comparable with the line ratio estimated for the BF transient AT2017bgt which is $F(\text{He II})/F(\text{H}\beta) \approx 0.5$ (Trakhtenbrot et al. 2019). The line intensities of He II $\lambda 4686$ and N III $\lambda 4640$ peak 2 days before the continuum peak, suggesting extreme ionization by UV/soft X-ray photons around the peak. The He II $\lambda 4686$ /He I $\lambda 5876$ ratio is sensitive to the change in the temperature and density as these lines belong to the same element but in two different ionization states (e.g., Ilić et al. 2009). We found the highest ratio close to the continuum peak, implying increased temperature in the BLR. The smallest ratio can be estimated from the post-flare-1 and late-time spectrum taken 315 days after the continuum peak that is due to a drop in the temperature.

5.1.3. Coronal lines

We detected several high-ionization coronal lines. Two of the detected coronal lines present already in the post-flare-1 spectrum taken 2 years after the first optical peak indicating a connection to the first optical flare.

Based on a study of SDSS spectra, Wang et al. (2012) reported the discovery of 7 Extreme Coronal Line Emitter (ECLE) galaxies which show extremely strong coronal lines. Three TDEs (AT2017gge, AT2019qiz and AT2022upj) were also found to have coronal lines (Onori et al. 2022; Newsome et al. 2022; Short et al. 2023). The BFF AT2021loi (Makrygianni et al. 2023) and the spectacular transient event AT2019avd (Malyali et al. 2021) have significantly detected coronal lines, too. Based on the

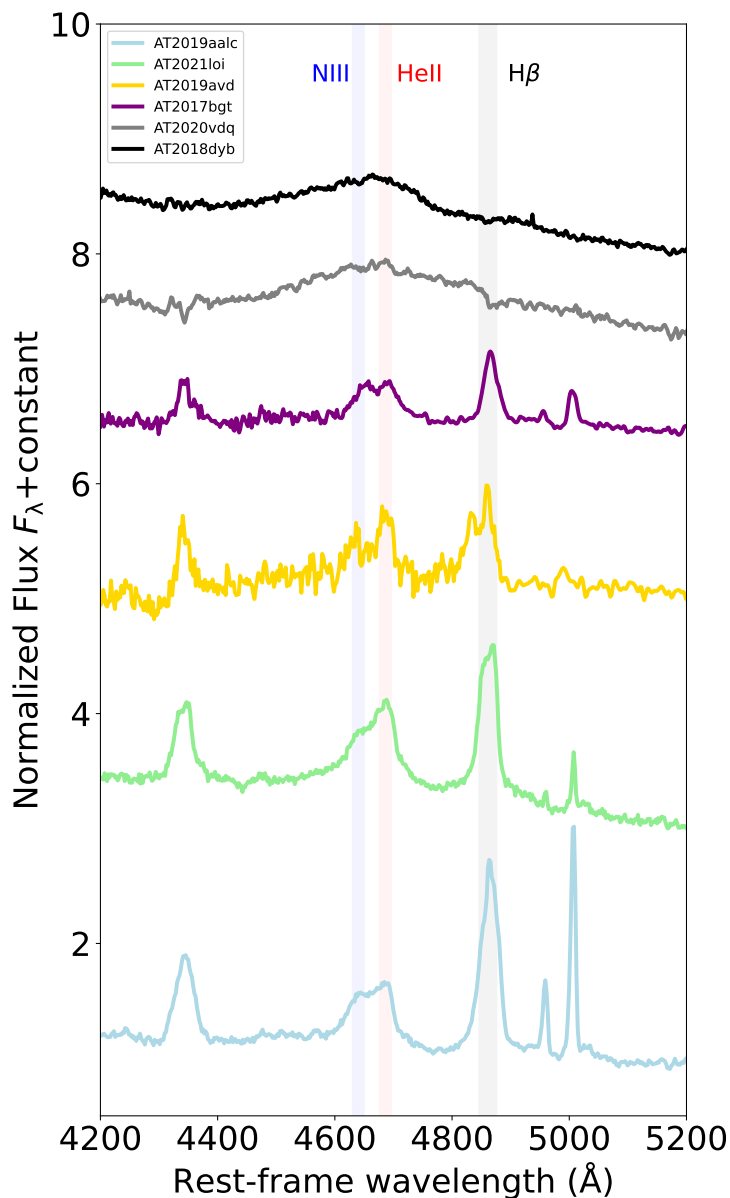


Fig. 15. The second LRS spectrum of AT2019aalc zoomed into the He II $\lambda 4686$ +N III $\lambda 4640$ doublet region compared to that of the BFFs AT2021loi (Makrygianni et al. 2023) and AT2017bgt (Trakhtenbrot et al. 2019), the peculiar transient event AT2019avd (Trakhtenbrot et al. 2020), the repeating TDE AT2020vdq (Somalwar et al. 2023) and the TDE-Bowen AT2018dyb (Pan et al. 2018). All of the plotted spectra were normalized at 5200Å.

publicly available spectra of AT2017bgt on the Transient Name Server¹¹ (TNS) we see enhanced coronal line emission in this BFF as well. Wang et al. (2012) states that the most possible origin of the ECLEs are remnants of an earlier TDE outburst which was later supported by Short et al. (2023) who revealed that the TDE AT2019qiz more likely follows the line ratio correlations of ECLEs instead of regular AGN. Interestingly, the coronal lines in AT2019qiz appeared around 400 days after the

optical peak, further supporting this scenario. Moreover, the estimated rate of coronal line emitters is consistent with the estimated rate of TDEs (Wang et al. 2012). According to Wang et al. (2012), the ECLEs could be explained through the coronal lines arising from Fe liberated from dust grains that were destroyed by the TDE flare. The large dust echo of AT2019aalc is consistent with this picture. Furthermore, the TDEs with coronal line detection clearly have more luminous IR dust echo compared to other optical TDEs. AT2019qiz is one of the few TDEs in-

¹¹ <https://www.wis-tns.org/>

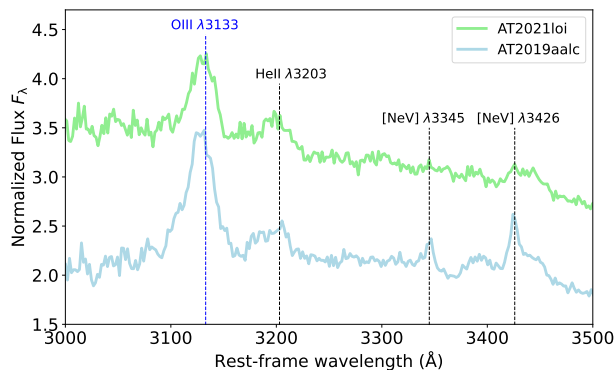


Fig. 16. The second LRIS spectrum of AT2019aalc zoomed into the O III λ 3133+He II λ 3203 doublet region compared to that of the BFF AT2021loi published by Makrygianni et al. (2023). The spectra were normalized at 5200Å.

cluded in the accretion flare sample of van Velzen et al. (2024) due to its strong dust echo. Another coronal line-detected TDE AT2017gge is part of the mid-infrared (MIR) dust echo flare sample of Hinkle (2024) which contains 19 ambiguous nuclear transients with high dust covering factors. The extreme dust echo seems to characterize the BFFs as well. The BFFs AT2021loi, AT2017bgt, OGLE17aaj and the candidate BFF AT2019avd are present in the above-mentioned MIR dust echo sample (Hinkle 2024) and 2 of them are also part of the Flaires sample of dust-echo-like IR flares (Necker et al. 2024). The Bowen line transient AT2019pev that shows strong high-ionization coronal lines (Frederick et al. 2021; Yu et al. 2022) is also part of the MIR flare sample of Hinkle (2024). These findings suggest a connection not only between the ECLEs and TDEs, but also the BFFs. Fig. 17 shows the [Fe x] λ 6375 versus the [O III] λ 5007 luminosities of the ECLEs studied by Wang et al. (2012), AT2019qiz (Short et al. 2023), two BFFs and AT2019aalc together with the SDSS Seyfert sample of Gelbord et al. (2009). This clearly implies an offset of the ECLEs, BFFs and AT2019aalc from the regular AGN sample.

The [Fe x] λ 6375 line evolution is shown in Fig. 18. The strength of this coronal line in AT2019aalc is further increased during the second flare and seem to be peaking lately with respect to the continuum peak. The coronal line TDE AT2019qiz shows a late-time increase in the this line as well (Short et al. 2023). Similarly to the case of AT2019qiz, we also found that [Fe x] λ 6375 line is the strongest high-ionization coronal line presented in the spectra, while [Fe VII] λ 6089 is the weakest one. The coronal line [Fe x] λ 6375 has been detected in several AGN before, however, the maximum line intensity ratio we calculated ($[\text{Fe x}]\lambda 6375 / [\text{O III}]\lambda 5007 \approx 0.65$) clearly overshoots the maximum ratio (≈ 0.24 , Nagao et al. (2000) found for AGN. For AT2021loi, Makrygianni et al. (2023) calculated even higher ratios, up to 2.06. The line width of [Fe x] λ 6375 shows a clear evolution during the monitoring of AT2019aalc as we estimated values of $\text{FWHM}([\text{Fe x}]\lambda 6375) = 1200 - 1800 \text{ km s}^{-1}$. Interestingly, the line widths we estimated for [Fe x] λ 6375 are clearly larger than the maximum values found for coronal line emitters (around 1000 km s^{-1} , Wang et al. 2012), however, very consistent with the width estimated for AT2021loi. For AT2021loi, Makrygianni et al. (2023) gives a line width of $\approx 2000 \text{ km s}^{-1}$ which implies that the line is consistent with a BLR instead of NLR origin since the latter would require the typical values estimated for coronal line emitters ($200 - 1000 \text{ km s}^{-1}$, Wang et al. 2012). The BLR

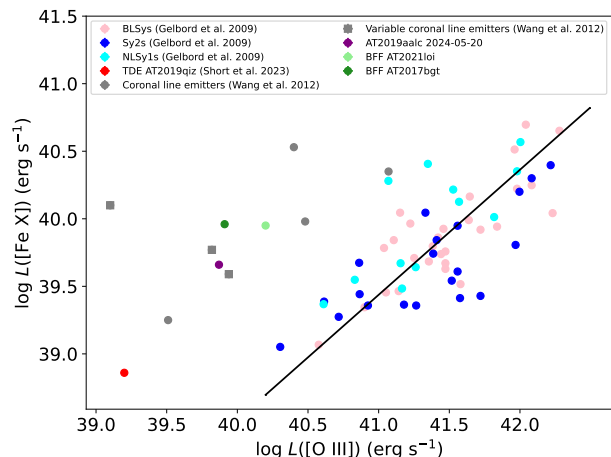


Fig. 17. [Fe x] λ 6375 versus [O III] λ 5007 luminosities of ECLEs, the TDE AT2019qiz (Short et al. 2023), two BFFs and AT2019aalc. A sample of different types of Seyfert galaxies (Gelbord et al. 2009) is plotted as well. The black line represents the mean ratio calculated for the sample. The transient sources have clearly higher [Fe x]/[O III] luminosity ratios than the Seyfert sample. Interestingly, the two BFFs, AT2019aalc and the TDE AT2019qiz all have significant dust echo emission and are presented in IR dust echo flare samples. This suggests that the coronal line emission can be explained via liberated Fe from the dust grains by TDE(-like) flares.

origin would naturally explain the increasing emission in these lines after the optical peak (due to the light travel time) but is also consistent with the distance between the dust responsible for the reprocessed IR emission and the SMBH ($0.1 - 1 \text{ pc}$, van Velzen et al. 2024). This suggests a connection between the unusually large dust echos and the extreme coronal lines in these transient sources. An alternative explanation is collisional excitation of these coronal lines. This is compatible with a detailed multi-wavelength study of AT2019qiz which suggests that outflows (powered by accretion or stream collision) are responsible for driving the optical flare of this coronal-line TDE (Nicholl et al. 2020).

The sulfur line [S XII] λ 7611 has the second highest ionization potential among the optical lines detected in AGN before (the highest one is [Ar XIV] λ 4412 which we do not detect in AT2019aalc). We zoom into the SPS fitted DBSP spectrum to show the detection of this line in Fig. 19. We can reasonably assume that the most recent and very strong X-ray flare, started less than a month before the appearance of the sulfur line, is responsible for the creation of this emission line. Apart from 5 ECLEs in the sample of Wang et al. (2012), [S XII] λ 7611 has only been reported in 4 Seyfert galaxies (Kraemer & Crenshaw 2000; Mazzalay et al. 2010; Cerqueira-Campos et al. 2021; Oh et al. 2022) including the neutrino emitter (IceCube Collaboration et al. 2022) NGC 1068 and in the nuclear transients VT J1548 (Somalwar et al. 2022) and AT2022fpx (Koljonen et al. 2024). VT J1548 is a radio-detected transient that was classified as a promising BFF candidate and notably with remarkable TDE-like characteristics (Somalwar et al. 2022). Similarly, AT2022fpx shares properties both with TDEs and BFFs (Koljonen et al. 2024). To our knowledge, AT2019aalc is so far only the third nuclear transient detected with a line requiring such a high creation ionization potential.

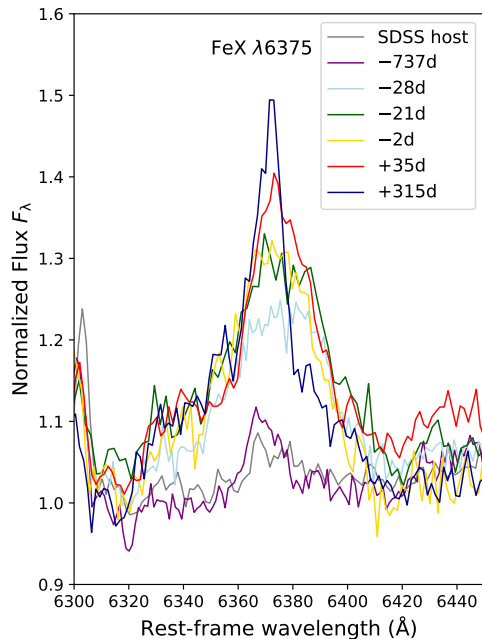


Fig. 18. The [Fe x] λ 6375 line evolution of AT2019aalc. The days in the legend are relative to the second optical peak.

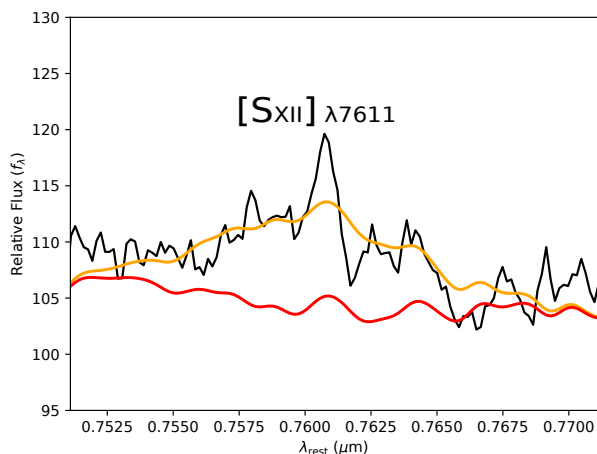


Fig. 19. The late-time DBSP spectrum taken almost a year after the optical peak of the second flare indicates the appearance of the high-ionization coronal line [S xII] λ 7611. The SPS fit (Subsect. 3.5.) of the spectrum allowed us to characterize this sulfur line.

5.1.4. Forbidden lines

We find evidence for the forbidden line [O III] λ 4363Å in the post-flare-1 LRIS spectrum and the late-time DBSP spectrum. Its detection, however, remains ambiguous because the Balmer line series are complex in our spectra, including blending from H γ . Nevertheless, the detections of [O III] λ 4363Å 2 years after the first flare and 1 year after the second flare is not unexpected. After all, this emission line requires densities much lower than the UV-line emitting clouds, and consistent with the outer NLR (or simple ISM) clouds (Ji et al. 2024) but is located inner than the emitting region of [O III] λ 5007Å (Nagao et al. 2001). The line

ratio of [O III] λ 4363Å/H γ \sim 1 suggests extremely hard ionizing radiation from the ionizing source. Using James Webb Space Telescope (JWST) observations, this line is sometimes detected and studied in detail in high- z AGN (used to distinguish AGN from star-forming regions), however, such a ratio was detected only in a very few cases (Übler et al. 2024; Ji et al. 2024; Mazzolari et al. 2024). The [O III] λ 4363Å/[O III] λ 5007Å ratio of \approx 0.7 is clearly higher than calculated for AGN which are typically below 0.2 (Baskin & Laor 2005; Übler et al. 2024; Binette et al. 2024)).

The highly ionized neon lines typically originate from star formation activity or photoionization of the EELR by the AGN. In some extreme cases, high-velocity AGN-driven shocks that ionize extended emission regions are expected to be responsible for the presence of the lines [Ne V] at 3345Å and 3426Å (Maddox 2018). The strengths of these lines in AT2019aalc are higher than the [O II] λ 3726+ [O II] λ 3729 doublets which indicate their origin related to AGN activity since [Ne V] is not excited by star formation (Maddox 2018). These shocks are possibly, but not exclusively, related to radio jets as high shock velocities of 900 km s $^{-1}$ are required to produce these lines (Maddox 2018). We estimated slightly lower velocities, which are therefore more consistent with the EELR origin and significant AGN photoionization in this outer region. From the increasing line intensities of [O III] and [Ne V] we can conclude that the NLR and EELR are also strongly ionized, however, in the late-time spectrum these decreased faster than the Bowen line N III λ 4640. The ionization level of the BLR is therefore more persistent than in the outer regions.

5.2. Optical re-brightening

The long-term ZTF light curve of AT2019aalc shows two well separated flares. Both flares evolved quickly and reached their peaks within 2 months, followed by a slow decay on yearly timescales. The first flare decayed for more than a year, while the second flare has been decaying for around a year.

Several ZTF monitored extragalactic transients have been found with bumps seen in their optical light curves (see Soraisam et al. (2022) for a recent review)¹². Most of them are SNe, however, a couple of them have been identified as TDEs (AT2020acka, AT2020nov and AT2021ehb). The latter two TDEs show prominent bumps in their light curves while decaying, while AT2020acka exhibits a long and monotonic bump. These TDEs are, however, experienced these bumps within a year from their peak. Moreover, the second flare of AT2019aalc peaked even at higher luminosities than the initial one. AT2020nov and AT2020acka experienced less significant second bumps, while AT2021ehb has two comparable peaks. The optical emission of these transients are poorly understood, and Soraisam et al. (2022) also states that their identifications as TDEs are ambiguous. Generally, TDEs are characterized by smoothly and rapidly declining light curves ($F \propto t^{-5/3}$ as expected from mass fallback considerations (Rees 1988) without any prominent bumps in the case of full disruption. AT2019aalc in turn has a slowly decaying first flare with a power-law fit returning a power-law index of $b \approx -0.45$ and a second flare that has started 4 years after the initial flare. The first systematically identified repeating partial TDE (AT2020vdq), however, shows not just a double-peaked long-term optical light curve,

¹² We note that ZTF has not been running long enough to discover flare repeats within longer timescales e.g., a decade that actually might also be common

but its second flare is ≈ 3 times more luminous compared to the first one (Somalwar et al. 2023). This implies an even more significant optical re-brightening than the one experienced by AT2019aalc. The second flares of partial TDEs are expected to follow an extremely steep $t^{-9/4}$ power-law when declining. In the case of AT2020vdq, the second flare declined much slower (Somalwar et al. 2023) than this but still clearly faster than the second flare of AT2019aalc which decayed with a power-law index of $b \approx -0.13$. Other candidate repeating TDEs have been found with periodic flares at different wavelengths; ASASSN 14ko with more than 20 observed optical/UV/X-ray flares (Payne et al. 2021), eRASS1 J045650.3-20375 with 3 X-ray/UV flares (Liu et al. 2023), AT2022dbl with two optical flares (Lin et al. 2024), while AT2018fyk (Wevers et al. 2019a, 2023) and RX J133157.6-324319.7 (Hampel et al. 2022) showed a one-time X-ray/UV and X-ray re-brightening episodes, respectively. In these cases, due to its grazing orbit, the star orbiting in the vicinity of the SMBH is thought to be only partially disrupted. After another pericenter passage, the surviving core thus feeds a new accretion flare, resulting in X-ray/UV re-brightening. For the Bowen-line and coronal-line emitter transient AT2019avd with two distinct optical flares, Chen et al. (2022) discusses a partial TDE scenario.

Interestingly, most of the sources of the small sample of classified BFFs show optical re-brightening or bumps. Fig. 20 shows the optical evolution of the three BFFs with detected re-brightening episodes together with AT2019aalc. The optical light curve of AT2017bgt shows a bump roughly 400 days after its initial flare which is also clearly seen in the binned light curve published in Trakhtenbrot et al. (2019). One of the two other BFFs originally studied by (Trakhtenbrot et al. 2019), F01004-2237, experienced a significant optical re-brightening around 11 years after its initial flare detected in 2010. Originally, Catalina Sky Survey (CSS) light-curve data revealed that this ULIRG had undergone a luminous continuum flare (Tadhunter et al. 2021) and later Trakhtenbrot et al. (2019) classified it as a BFF similar to AT2017bgt. The binned light curve of this source published in Makrygianni et al. (2023) shows a bump around a year after its peak. We investigated the recent activity of the source and found that it significantly re-brightened in 2021 based on its ATLAS monitoring. The recent flare was more luminous than the first one and decayed faster. In addition to these two BFFs, AT2021loi shows a bump during its decaying, roughly a year after the first flare reached its peak. Makrygianni et al. (2023) suggests that optical re-brightening or bumps seen when decaying might be common features of BFFs. Only one transient classified as a BFF, OGLE17aaj, has not shown signs of optical re-brightening or bumps in its light curve to date. The first flares of the studied BFFs decay on yearly timescales, i.e. much slower than TDE flares but more similar to AT2019aalc. However, the BFFs with re-brightening episodes tend to have a faster decaying second flare/bump in comparison with their initial flare, while in the case of AT2019aalc the second flare decays slower. The BFFs classified so far tend to have remarkable variances in their optical light curve evolution in addition to the similarities we see. These might be explained by different subclasses of BFFs, similarly to regular TDEs, where different subclasses have been defined based on their light curve evolution (e.g., Charalampopoulos et al. 2023).

5.3. Possible explanations of the long-term radio flare

In this subsection we discuss the long-term radio variability of AT2019aalc. The source experienced a brightening of its flux

density by a factor of 2 on a timescale of less than 1.5 years followed by a long-term plateau (≥ 3 years) indicated by the archival radio survey data and our ATCA monitoring. Although radio variability on yearly timescales is a common phenomenon of Seyfert galaxies, the sharp, high-amplitude radio flare and especially the long-term plateau are generally not seen in intrinsically variable Seyfert galaxies (e.g., Mundell et al. 2009; Koay et al. 2016) and therefore require further investigation. The unusual radio spectrum with a high frequency turnover is also discussed below.

- The brightness temperature of $T_b = (3.0 \pm 0.8) \times 10^9$ K at 1.7 GHz significantly exceeds 10^5 K, known as an upper limit for supernova remnants and He II regions in star-forming galaxies (Condon 1992). Consequently, the radio emission we detected must be non-thermal and originate from physical processes associated to AGN-like (including TDEs) activity (see Bontempi et al. 2012 as an example how the estimated brightness temperatures help to characterize the radio emission of Seyfert galaxies). This way, we can also safely rule out thermal free-free emission from the accretion disk or the dusty torus (e.g., the case of NGC 1068, Gallimore et al. 1997) as the origin of the detected radio emission.
- Advection-dominated accretion flows have also been proposed to explain the origin of the radio emission of low-luminosity AGN (e.g., Seyfert galaxies, Mahadevan 1997). Assuming that accretion flows dominate the radio emission of AT2019aalc, following Yi & Boughn (1998) we estimate an expected 5 GHz radio luminosity of $\approx 4 \times 10^{35}$ erg s $^{-1}$, a magnitude of 3 lower than the observed one, clearly indicating that the advection-dominated accretion flows cannot explain the observed radio emission in our case.
- Magnetized coronal winds originating from the AGN accretion disk could produce the non-thermal radio emission of AT2019aalc. Laor & Behar (2008) found a correlation of $\log(L_R/L_X) \approx -5$ studying the Palomar–Green (PG; Green et al. 1986) radio-quiet quasar sample (in good agreement with the correlation found for coronally active stars by Guedel & Benz (1993). Later, Behar et al. (2015) came to the same conclusion using a sample of seven radio-quiet Seyfert galaxies. Magnetized coronal winds were proposed to explain the observed radio emission of the Seyfert galaxy Mrk 590 by Koay et al. (2016), however, the authors noted that a jet contribution cannot be ruled out. These two types of outflows might even be equivalent and cannot be distinguished in Seyfert galaxies with unresolved compact core features seen in their VLBI maps (e.g., Kharb et al. 2015), like in the case of AT2019aalc. For our source, based on the mean ATCA C-band and the extrapolated *Swift*/XRT 2 – 20 keV luminosities, we estimate a ratio of $\log(L_R/L_X) \approx -2$ suggesting that magnetized coronal winds alone cannot fully explain the observed radio emission of AT2019aalc. Moreover, coronal emission should be rapidly variable at radio wavelengths and should evolve similarly to the X-ray flux, which is clearly not the case. Although, a contribution from the mechanisms discussed so far to the total radio flux remains a possibility, we need to look for another possible origin to explain the main origin.
- Out-flowing synchrotron emitting material induced by enhanced accretion are commonly detected in AGN and TDEs in the forms of non-relativistic outflows or relativistic jets which can be either on or off-axis relative to the observer. These features are often visible on VLBI radio maps of radio-detected Seyfert galaxies (e.g., Kozák et al. 2024) and

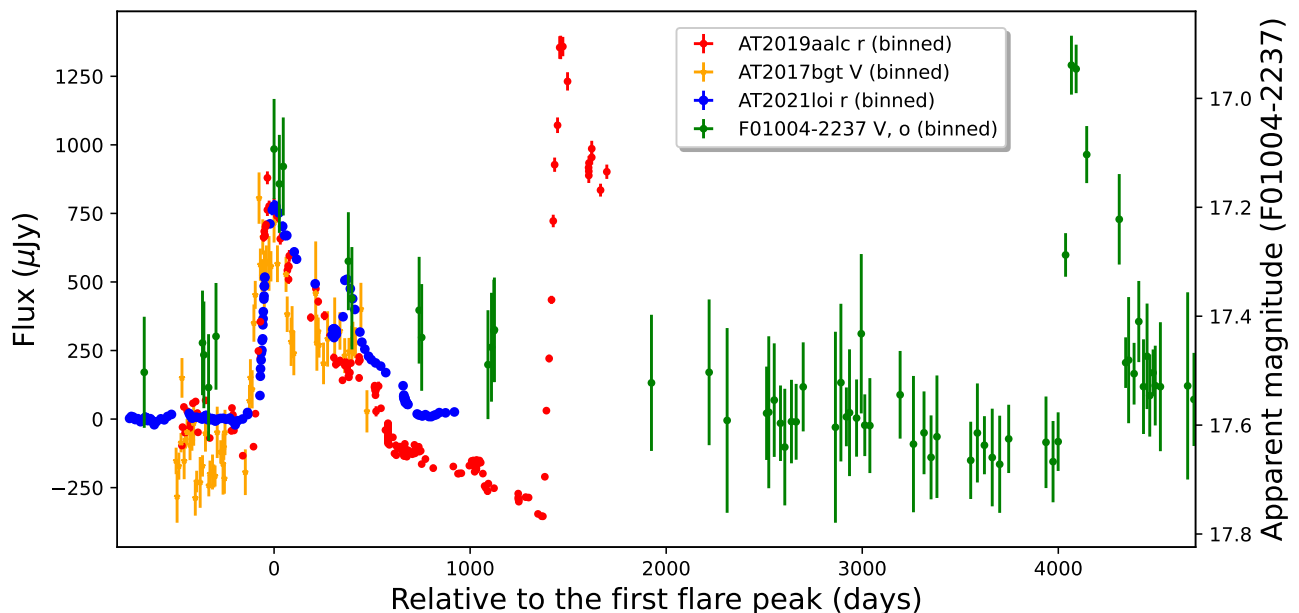


Fig. 20. Long-term optical light curves of AT2019aalc and three classified BFFs. The light curves indicate that optical re-brightening and bumps may be a common property of BFFs; yet, the various sources differ in when these episodes start with regard to the initial flares.

a few TDEs (e.g., Paragi et al. 2017; Mohan et al. 2022). In our case, the high brightness temperature of the EVN-detected radio feature together with its position (in good agreement with the optical *Gaia* position) indicate its radio core identification, however, no other components were detected. Nevertheless, the steep ($\alpha \ll -0.5$) radio spectrum revealed by our ATCA observations indicates the presence of another, steep spectrum synchrotron-emitting component(s) in the system as radio cores are characterized by a flat radio spectrum. The steep radio spectrum may be the composition of the flat spectrum radio core and the additional, steep spectrum component(s). The ATCA radio spectrum indicates a high-frequency turnover above 9 GHz which is a possible hint of a newly ejected radio-emitting component. We further discuss the radio spectrum of AT2019aalc in the following.

The turnover suggests the multiple component nature of the spectrum. Radio spectra with high-frequency excess have been observed in a few radio-quiet narrow-line Seyfert 1 galaxies (Berton et al. 2020). These sources are thought to be kinematically young AGN with small linear sizes or heavily absorbed AGN. The high-frequency peak might be explained with the kinematic age of a newly ejected component. Since older sources are larger than young ones, the expanding relativistic jet or non-relativistic outflow loses energy as the density decreases and the spectral peak moves to lower energies over time. With other words, as the projected linear size of the radio source increases, the turnover frequency decreases. These extremely young radio sources therefore peak at very high frequencies (e.g., Berton et al. 2020). The low-frequency peak is, however, more likely to be explained with star formation activity (as NLSy1 galaxies have a significantly higher star formation rate as other AGNs) instead of AGN emission. The latter is assumed to be synchrotron self-absorbed (SSA) to explain the faintness or the non-detection of these galaxies at lower frequencies. As another possibility to explain the high-frequency excess of, Berton et al. (2020) dis-

cusses a scenario in which the AGN emission is absorbed below 10 GHz due to free-free absorption (FFA). In that case, the circumnuclear gas might be ionized both by the AGN and by hot stars and might act as a screen for the jet at low frequencies or the passage of the jet in the interstellar medium causes the formation of a cocoon of ionized gas and this way being responsible for the FFA. Finally, coronal emission could also be responsible for the inverted spectrum.

In the case of AT2019aalc, the coronal emission scenario can be safely excluded as we should see a rapidly variable radio light curve which should evolve similarly to the X-ray emission. On the other hand, the other two scenarios might also be challenging. The large-amplitude variability concluded from the VLASS observations and the EVN detection of a high brightness temperature ($T_b \gg 10^5$ K) feature at 1.7 GHz clearly imply AGN-like activity over a star formation scenario at these frequencies and is incompatible with significant absorption caused by SSA or FFA. Moreover, the presence of a relatively strong [O III] $\lambda 5007$ line in the SDSS host spectrum implies earlier AGN activity as being responsible for the radio emission before the long-term flare. Therefore, our results indicate that the radio spectrum of AT2019aalc is strongly dominated by AGN activity below 10 GHz as well, even if a contribution from star formation, especially at 2.1 GHz, is probable.

Nevertheless, the contribution of a newly ejected component to the overall radio spectrum remains a possibility. In the cases of the earlier discussed NLSy1 galaxies, the high frequency peak is thought to be suggesting a newly born radio source with no signs of earlier jet activity. Similarly to gigahertz-peaked sources (GPS), the high-frequency peak is thought to be shifting towards lower energies over time. This way, NLSy1 galaxies might be extremely young GPS which was first suggested by Oshlack et al. (2001). In our case, a newly ejected component can be responsible for the high-frequency excess whilst the low-frequency part is naturally explained with optically thin synchrotron emission of the AGN indicating that we do not see a newly born radio-

AGN but an AGN with recently enhanced, intermittent activity. The result is a two-component radio spectrum with a relatively steep spectrum at lower frequencies and a high-frequency excess. The steepness of the spectrum between 888 MHz and 9 GHz might be explained with cooling of electrons originating from past AGN activity, and also a contribution from star formation can play a role here. Järvelä et al. (2021) states that restarted AGN activity can explain at least some of the radio spectra studied by Berton et al. (2020). The broad-line AGN classification of the host galaxy of AT2019aalc is more consistent with a restarted AGN picture as this type of AGN are thought to be older than NLSy1s making a restarted activity scenario over a newly born radio source one more probable. The restarted activity results in a peaked spectrum at higher frequencies, superimposed on a spectrum from a period (or periods) of earlier activity peaking at lower frequencies. Intermittent activity is further supported by theoretical models suggesting that sources with high accretion rates are more prone to this kind of behavior (Czerny et al. 2009). This is compatible with the accretion-induced lines seen in the post-flare-1 optical spectrum of AT2019aalc (see Subsubsection 4.5.2 and van Velzen et al. 2024).

We note that the fitted ellipsoid model fit component to the EVN visibility data is aligned to the northwest-southeast direction (clearly differs from the position angle of the restoring beam indicating the angle-dependent resolution of the VLBI array) which potentially indicates a newly ejected radio-emitting component. Higher frequency observations with improved angular resolution are required in order to resolve the radio structure we detected at 1.7 GHz. We observed AT2019aalc with the EVN and the Korean VLBI Network (KVN) jointly at 21 GHz in March 2024 and expect to reach sub-mas-scale angular resolution, roughly an order of magnitude better than with the currently discussed observation. These results will be presented in a follow-up publication (Veres et al. in prep.)

5.4. X-ray properties

The X-ray spectra of AGN at energies above 2 keV have a power-law-like shape. These X-ray photons are believed to be triggered by Compton up-scattering of the accretion disk photons off hot electrons surrounding the disk, in a hot ($\approx 10^9$ K) optically thin corona above the disk (e.g., Kammoun et al. 2015). Below 2 keV energies many AGNs show an excess in their spectrum referred to as the soft X-ray excess. This soft excess can be well modeled by a blackbody model with a best-fit temperature in the range 0.1 – 0.2 keV. The origin of the excess might be explained via Comptonized disk emission and the reflection of hard X-ray photons from the surface of the disk can account also for the excess (Done et al. 2012).

The stacked *Swift*/XRT X-ray spectrum of AT2019aalc can be adequately described with an absorbed blackbody+power-law model. We note that in the cases of strongly beamed jetted sources e.g. blazars, the X-ray spectrum can be well modeled with a simple or broken power-law without adding any additional model component (e.g., Kammoun et al. 2015; Acciari et al. 2022). Although AT2019aalc shows enhanced radio activity, its brightness temperature suggests a non-beamed nature of its radio emission in agreement with the X-ray spectrum.

The X-ray spectrum is dominated by a power-law component with a soft power-law index of $\Gamma \approx 2.8$ while the thermal component is extremely soft with a blackbody temperature of $kT \approx 90$ eV derived from the *Swift*/XRT observations. Most of the BLSy1s typically have a significantly harder X-ray spectrum with a power-law index $\Gamma = 1.7 - 2$ (e.g., Pons & Watson 2014).

Our value is more typical for sources characterized by enhanced accretion, e.g., flaring NLSy1s or TDEs which have typically soft X-ray spectra with $\Gamma > 2$ (Boller et al. 1996; Saxton et al. 2020).

The soft X-ray excess appears in the stacked spectrum and becomes more significant over time as we added a blackbody component in order to better describe the X-ray spectrum. Furthermore, the data of the peak of the second X-ray flare is clearly better-fit with a single blackbody model than with a power-law one (Subsect. 4.3) implying not just the need of the blackbody component to adequately fit the data but even its dominance over the power-law component at this epoch. A softening of the power-law index over time can be seen as well. These results suggest significantly enhanced accretion or disk instability. Delayed accretion flares have been observed in TDEs (Saxton et al. 2020). In our case, the post-flare-1 spectrum shows clear signs of accretion and the second flare is followed by enhanced accretion activity as well.

The soft X-ray flux of Seyfert galaxies was found to be well correlated with the observed fluxes in the coronal line [Fe x]. The coronal lines to X-ray flux ratio is $\log(f_{[\text{Fe x}]} / f_x) = -3.43 \pm 0.55$ for both broad and narrow-line Seyfert 1 galaxies (Gelbord et al. 2009). For AT2019aalc we estimate values of $\log(f_{[\text{Fe x}]} / f_x) \approx -3.45$ when optical spectroscopic and X-ray observations were performed nearly simultaneously (due to the rapid X-ray variability we consider only observations taken on the same day). This implies that the expected soft X-ray luminosity is consistent with the observed values. The soft X-ray photons excite the coronal lines continuously and not years later originating from a past TDE as it was suggested for ECLEs by Wang et al. (2012). The photoionization or collisional excitation of the dust grains is rather due to a current event. This further supports that the re-occurring optical/UV outbursts seen during the decaying of the flares are driven by the soft X-ray flares which lead these outbursts only with a couple of weeks. These suggest an accretion-driven origin of the reoccurring outbursts in the optical/UV during the decaying of the flare.

5.5. SED fitting

Following Reusch et al. (2022), we fitted two blackbody models in order to describe the SED of the transient using `LMFIT`. These fitted curves to the optical/UV ('blue' blackbody) and IR data-points ('red' blackbody) are shown in Fig. 21, together with a combined double blackbody fit. The red blackbody fit was introduced to account for the IR dust echo. These curves fit the SED around the optical peak of the investigated flare.

The continuum emission of TDEs are well described by a thermal blackbody model (Gezari 2021). The case of AT2019aalc appears to be more complex. An excess in the UW2 band can be seen regardless the consideration of a simple or the double blackbody fit. The UV emission have a contribution from the Bowen Fluorescence mechanism and potentially also from Comptonization explaining the poor fit towards the blue. The red wing of the optical and the IR part cannot be well fitted with a simple blackbody model suggesting a complex, multi-component dusty reprocessing region. The excess in the *r*-band might be explained with the early appearance of some Fe lines in this range (such as [Fe x] λ 6375 and [Fe vii] λ 6088) indicating the release of this element previously locked up by the dust grains. Since all of this seem to be started already around the optical peak, at least a fraction of the dust is located on \sim subpc scales to the SMBH. This is further consistent with the extreme line widths of the coronal lines (see Subsect. 5.1.3). Therefore, not

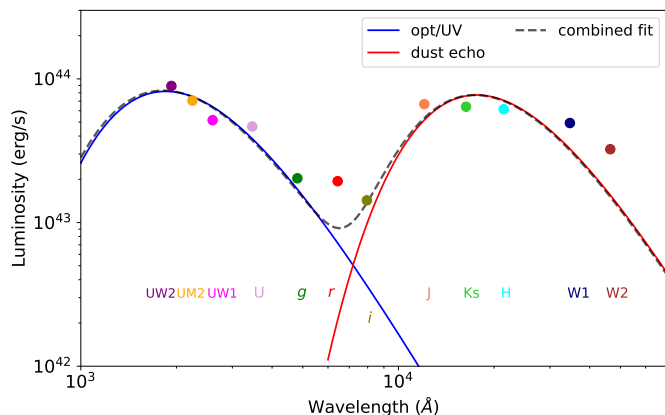


Fig. 21. The extinction-corrected SED of the second flare of AT2019aalc as measured around the optical peak. Two blackbody models to the optical/UV (blue curve) and IR datapoints (red curve) were fitted separately and a combined fit (black dashed curve) is also shown. A clear excess in r -band and the WISE bands can be seen.

only the dusty tori is responsible for the IR dust echo. It is possible that the significant amount of dust in the nucleus region is the consequence of enhanced star formation sometime in the past. The Baldwin, Phillips & Terlevich (BPT, Baldwin et al. 1981) emission-line ratio diagnostics of the host SDSS spectrum are $\log([\text{O III}] \lambda 5007/\text{H}\beta) \approx 0.3$ and $\log([\text{N II}] \lambda 6583/\text{H}\alpha) \approx -0.4$. We plotted the BPT line-ratio of SDSS spectra with indicating the ratios of the host galaxy of AT2019aalc and the BFFs AT2021loi, AT2017bgt and F01004-2237 in Fig. 22 using `ASTROML` (Vanderplas et al. 2012; Ivezić et al. 2014). All of the investigated galaxies are in the composite region, consequently, in addition to AGN activity, star formation activity might also have a remarkable contribution for producing the narrow lines seen in the spectra. Moreover, these ratios place these two galaxies solidly in the region of the diagram where the post-starburst sample of French et al. (2015) is located. We note that to derive the ratios for AT2019aalc and F01004-2237, we used pre-flare spectra. While as no host spectra are available for AT2017bgt and AT2021loi, we considered the spectra taken as early as possible in these cases.

5.6. What type of transient is AT2019aalc?

AT2019aalc shares similarities with TDEs such as the soft X-ray spectrum, the dust echo and the optical flare(s) rising with constant color. The UV bright nature of the transient with a blue optical/UV peak color of $\text{NUV}-r \approx 0.2$ is another TDE-like feature and not typical for AGN and SNe (Gezari 2021). Bowen lines appear in the spectra of several TDEs even if these are typically weaker than in our case. The most remarkable difference is, however, the decay of the optical emission, which is significantly slower than for any TDE identified so far. The color evolution of the flares is also typical for TDEs.

The unobscured AGN-like optical spectra, the presence of persistent and strong Bowen lines ($\text{O III } \lambda 3133$ and $\text{N III } \lambda 4640$), the extremely luminous UV flare, on yearly timescales decaying optical emission and the optical re-brightening altogether suggest a Bowen Fluorescence Flare classification of AT2019aalc. Furthermore, we classify AT2019aalc as an Extreme Coronal Line Emitter because of the detection of strong high-ionization coronal lines.

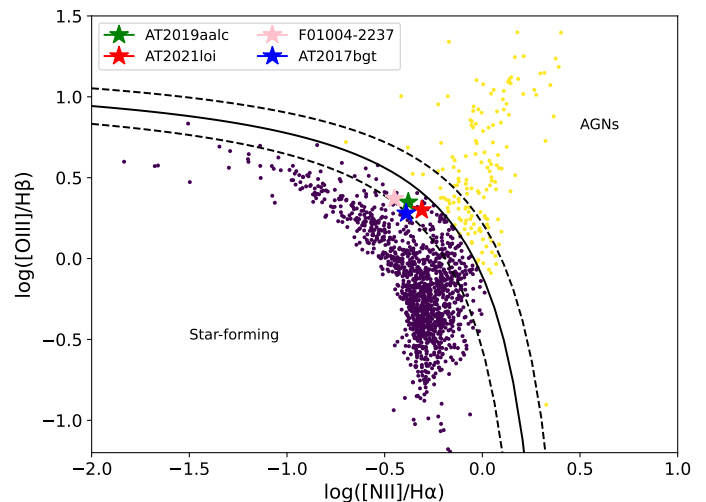


Fig. 22. The BPT narrow line ratio diagram (Baldwin et al. 1981) of SDSS spectra. The location of the dividing line is taken from Kewley et al. (2001). The dashed lines represent the composite region i.e. where both star formation and AGN activity play a role. The line ratios of the host galaxy of AT2019aalc derived from the fitted SDSS spectrum are indicated with a green star symbol. For the BFFs AT2021loi and AT2017bgt the ratios are taken from Makrygianni et al. (2023) and Trakhtenbrot et al. (2019) and indicated with red and blue star symbols, respectively. To derive the ratios for the BFF F01004-2237, we downloaded its 6df (Jones et al. 2009) spectrum which was taken years before the first flaring episode of the transient. The location of the BFFs in the diagram suggests remarkable current or past star formation activity which might explain the extreme dust echo emission of the transients.

The mechanism that powers the long-term accretion enhancement in BFFs is still unclear. TDEs in AGN might play a role. In a single star case, the slowly decaying optical/UV emission might be explained by the dissipation of energy due to the interaction between the stellar debris stream and the pre-existing accretion disk (similarly to the case of the TDE-AGN PS16dtm, Blanchard et al. 2017) or the AGN's radiation field. The bumps in optical and UV during the decay of the flares of AT2019aalc led by soft X-ray flares indicate the flare's accretion-driven origin consistently within this picture. Moreover, the flaring episodes in X-rays seem to be happen periodically which is expected from interaction between a circularizing stellar stream and the accretion disk. The origin through reprocessing is further consistent with the ionization of the BLR and so on the increase in the Bowen and the Balmer lines seen in the spectra during the second flare. The dusty region (expected from a source with IR dust echo) and the liberation of Fe and S from these dust grains due to photoionization by the soft X-ray flares provide an explanation for the high-ionization coronal lines. The increase of the W1–W2 color implies significant cooling expected from cooling dust after the onset of the dust echo. This scenario provides explanation for one slowly decaying flare with recurring outbursts, however, AT2019aalc exhibits two distinct optical flares. The second flare is even more luminous than the first one, similarly to the case of the partial TDE AT2020v dq (Somalwar et al. 2023). A partial TDE scenario might explain the second optical flare.

Although the slowly decaying optical emission and the re-brightening seem to be common features of BFFs, the long-term light curves still show differences as well. The re-brightening

episodes started at different timescales for the individual sources, and more BFFs need to be classified to better understand their unique optical light curves. Nevertheless, (partial) TDEs occurring in AGN can be a possible origin of BFFs. This would explain the TDE-like properties of these sources. The most remarkable differences i.e. the slowly decaying optical emission and the continuum emission not being well described by blackbody models might appear due to a more complex environment the TDE takes place with comparing to quiescent galaxies. Furthermore, a possible connection between the high-ionization coronal lines (which are most probably related to TDE activity, Wang et al. 2012) and the BFFs is consistent with this picture. A known potential partial TDE in an AGN is the case of the active galaxy IC 3599. This low-luminosity AGN exhibits periodic soft X-ray flares interpreted with a partially disrupted star, which results in reoccurring outbursts after each passage of the surviving core around the central black hole (Campana et al. 2015). Notably, IC 3599 has more prominent high-ionization coronal lines than most AGN (similarly to the coronal-line detected transients, see Fig. 17). Interestingly, IC 3599 is the only known AGN with fading coronal lines (Frederick et al. 2019).

Alternatively, a double TDE i.e. the tidal disruptions of a pair of binary stars might explain the double-peaked optical light curve. Notably, double TDEs may represent nearly 10% of all stellar tidal disruptions (Mandel & Levin 2015).

The strength of the high-ionization coronal lines that regular AGN activity cannot explain the unusual behaviour of this transient. It is not clear why we do not see as strong high-ionization coronal lines in normal AGNs as in the transients with significant dust echo emission i.e. TDEs and BFFs. It might be explained with dust sublimation due to the UV radiation of the AGN (the sublimation radius is typically in the subpc range, van Velzen et al. 2021b) which clears the dust from the nucleus region. AGN-driven outflows play also a role here. The limited variability of the host galaxy of AT2019aalc prior the first flare and its location in the BPT diagram suggest weak AGN activity before the transient occurred. Therefore, the dust possibly originating from star formation activity in the nucleus could survive. Additionally, the first flare could not clear the nucleus region which suggests that it must have been way less luminous in UV than the second flare. Unfortunately, due to lack of UV data around the first flare this hypothesis cannot be further tested. Nevertheless, the detection of some Fe lines in the post-flare-1 spectrum implies that a certain fraction of the dust was destroyed following the first flare.

Interestingly, the host AGN of other BFFs also showed weaker pre-transient activity than persistently accreting AGN (Trakhtenbrot et al. 2019; Makrygianni et al. 2023). The TDE-like features suggest that TDEs might restarted these AGN. Beyond the TDE-related scenarios, it is possible that the restarted AGN activity is rather explained with the dusty environment itself.

As we studied AT2019aalc in radio in detail, we compare the radio properties with that of the BFFs available. Based on the radio observations explained in Makrygianni et al. (2023) AT2021loi has an inverted radio spectrum between 5 and 10 GHz while the source was not detected at 3 GHz which can be compatible with a newly ejected jet or outflow component, similarly to the case of AT2019aalc. Although no radio spectrum is available for AT2017bgt, we investigated the VLASS QL Images of this BFF to study its radio flux variability. We found a radio source at the optical position of AT2017bgt with flux densities of 3.6 mJy (on 2019-05-21), 6.6 mJy (on 2021-10-19) and 4.5 mJy (on 2024-06-11) at a central frequency of 3 GHz.

The host galaxy of AT2017bgt was detected in the FIRST (at 1.4 GHz) in July 1998 with a flux density of 0.9 mJy. In addition, the BFF candidate VT J1548 was also found to exhibit a radio spectrum peaking around 5 GHz (in contrast with non-jetted AGN that peak below 1 GHz, e.g., Padovani et al. 2017) which was explained with an ejection of a synchrotron-emitting outflow (Somalwar et al. 2022). These findings allow us to conclude that newly ejected radio outflow/jet components play a crucial role in BFFs. These outflows ejected due to enhanced accretion might be partly responsible for the liberation of Fe and S from the dust grains located relatively close to the SMBH. The collisional ionization in the case of AT2019aalc is supported by the extreme broadness of the coronal lines especially [S XII] λ 7611.

5.7. BFFs and high-energy neutrinos

AT2019aalc has been associated with the high-energy neutrino event IC-191119A (most probable neutrino energy: 177 TeV) detected by the IceCube Observatory (IceCube Collaboration 2019; van Velzen et al. 2024). Motivated by the classification of AT2019aalc suggested by its multi-wavelength properties (Subsect. 5.6), we searched for spatial coincidences between the earlier classified BFFs and the neutrino alerts from the IceCube Event Catalog of Alert Tracks (ICECAT-1; Abbasi et al. 2023). We found that the BFF AT2021loi is located within the 90% rectangular uncertainty contour of the high-energy neutrino event IC-230511 (most probable neutrino energy: 167 TeV) detected in May 2023 (IceCube Collaboration 2023). In the full likelihood contours published in ICECAT-1, the source is just outside the 90% contour. We present the source positions together with the neutrino best-fit positions and both contours in Figs. 23 and 24. We also report a coincidence between the 'prototype' BFF AT2017bgt and the high-energy neutrino event IC-200410A. This event is, however, a poorly reconstructed cascade event, therefore we do not discuss it further here.

The neutrino associated with AT2021loi is 680 days delayed with respect to its first optical peak and 290 days with respect to its second optical peak. Note, that the 3 nuclear transients (including AT2019aalc) are associated with neutrinos that were delayed by 150 – 290 days, which might be explained with delayed mass accretion, delayed jet formation or outflow ejection (van Velzen et al. 2024). In the case of AT2021loi, the inverted radio spectrum (Makrygianni et al. 2023) is compatible with a newly ejected jet or outflow component, similarly to the case of AT2019aalc. However, from the current data, we cannot tell if the radio-emitting region of AT2019aalc has been ejected before or after the neutrino. Although we do not see a clear increase in the 888 MHz RACS data 6 months after the neutrino arrival. However, if the radio flare is indeed related to a newly ejected, synchrotron self-absorbed component, it is not surprising that it does not result in any increasing at low frequencies at early times. Interactions between the out-flowing material and clouds in the surrounding of the SMBH (Wu et al. 2022) or between ultra-high energy protons (accelerated in a jet or outflow) and infrared photons from the dust echo (Winter & Lunardini 2023) were proposed to explain the observed neutrino emission of the 3 nuclear transients. These findings indicate that outflows play an important role in the neutrino production. Moreover, Winter & Lunardini (2023) estimate the highest neutrino fluence for AT2019aalc among the 3 studied nuclear transients associated with neutrinos. A similar case study for AT2021loi would help us to further constrain the neutrino production models of nuclear transient sources.

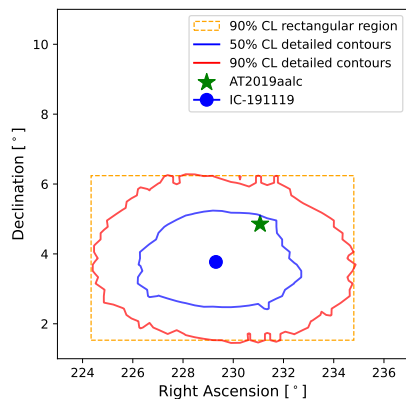


Fig. 23. The blue and red contours represent the 50% and 90%CL containment detailed contours of the high-energy neutrino event IC-191119A, respectively. The orange box is the 90%CL rectangular containment region. The neutrino best-fit position is shown with a blue point. The optical position of AT2019aalc is marked with a green star sign. This coincidence was originally published in [van Velzen et al. \(2024\)](#). The detailed contours are presented here for the first time.

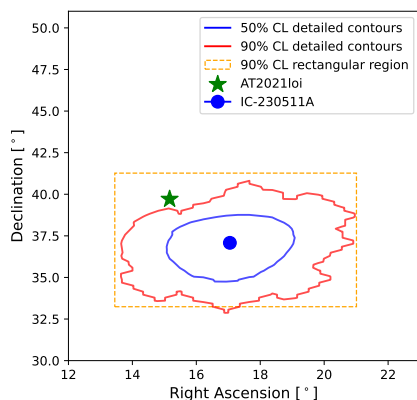


Fig. 24. The blue and red contours represent the 50% and 90%CL containment detailed contours of the high-energy neutrino event IC-230511, respectively. The orange box is the 90%CL rectangular containment region. The neutrino best-fit position is shown with a blue point. The optical position of AT2021loi is marked with a green star sign.

If the connection between the high-ionization coronal line detection and the unusually large dust echos of nuclear transients is real, this can be used to reveal more sources with strong dust echo and therefore more candidate neutrino sources. Notably, both AT2019aalc and AT2021loi are characterized by significant dust echos ([van Velzen et al. 2024](#); [Hinkle 2024](#); see also Subsect. 4.2) and unusually strong high-ionization coronal lines ([Makrygianni et al. 2023](#); see also Subsect. 5.1).

6. Conclusions

We conducted a multi-wavelength campaign during the second optical flare of the nuclear transient AT2019aalc associated with a high-energy neutrino event. We found that the second optical flare is even more luminous and decays even slower than the first one. Both flares evolve rapidly and with constant color. The optical flare is accompanied by UV emission which peaks at extremely high luminosities (at $\approx 10^{44}$ erg/s). The IR emission in-

creases, similar to the first flare when it peaked delayed with respect to the optical and was explained with a dust echo flare. We detected a very soft X-ray flare that peaked before the optical/UV emission peaks. Later, the *Swift*/XRT detected an almost 10 times more luminous X-ray flare which is clearly dominated by a blackbody component, suggesting enhanced accretion or disk instability.

Our VLBI observation provides a hint of extension of the radio-emitting source and clearly favors an AGN-like origin over a star-formation scenario. The radio monitoring revealed a long-term flare and an inverted spectrum above 9 GHz, which is most probably explained by a newly ejected, self synchrotron-absorbed outflow or jet component. As we do not see obvious signs of variability well before the first optical flare, we suggest that the transient event in 2019 renewed the activity of the host AGN. Restarted AGN tend to have inverted radio spectrum. This also naturally explains the long-term flare.

The results from optical spectroscopy help us to better understand the event responsible for restarting the AGN. In the optical spectra, the presence of persistent Bowen lines are consistent with intensified accretion over a year after the second flare. The UV bright nature of the transient is consistent with the Bowen mechanism which pumps lines mostly in this range. The line intensities of the Bowen lines and the temperature of the BLR both peak around the peak of the optical flare indicating that the optical flare is driven by the ionization of the clouds of most probably the BLR. As we find the X-ray flaring episodes prior to the rise in optical/UV, the origin of the latter is most probably reprocessed X-ray photons which are also required for the extreme ionization implied by the Bowen lines. The X-ray flares are very soft which explains the unusually strong He II lines. These findings altogether suggest the accretion-driven origin of the flaring episode we monitored. Note, that reprocessed soft X-ray emission i.e. by an outflow surrounding the disk is a possible explanation for the origin of the optical/UV emission of TDEs ([Bu et al. 2022](#)).

We detected several persistent or even late-time increasing high-ionization coronal lines in the spectra of AT2019aalc. The detection of $[S\text{ XII}]\lambda 7611$ requires an extremely high ionization potential. To our knowledge, AT2019aalc is only the third extragalactic transient event detected with this line and only 4 Seyfert galaxies (including the neutrino emitter NGC 1068) and 5 ECLEs were reported with a line with such a high ionization potential. The Fe/X-ray ratios disfavor a past TDE interpretation responsible for the coronal lines, which was proposed to explain these lines seen in most of the ECLEs studied earlier. The slowly decaying optical emission might instead be explained with continuous photoionization of the dust grains (located at distances consistent with the BLR instead of the NLR as seen for ECLEs before). This is consistent with the early observation of the dust echo emission with respect to the optical peak which suggests that the dusty region is located very close to the SMBH. Based on the narrow-line ratios, we found that enhanced star formation activity is a favorable explanation for the dusty environment. Moreover, the gas-rich environment might explain the restarted activity of the AGN.

The high $[\text{Fe X}]\lambda 6375 / [\text{O III}]\lambda 5007$ luminosity ratios of the BFFs, coronal line-detected TDEs and ECLEs suggest a possible connection between these source types. These sources tend to have large dust echo-like flares, which implies that the liberation of Fe from the dust grains can be explained via their TDE(-like) flaring episodes. The significant photoionization is supported by the detection of strongly ionized neon lines in the EELR. A delayed outflow/jet component and collisional excita-

tion provides an alternative explanation for the coronal lines and their late-time increasing or appearance. The BFF and coronal-line emitter AT2021loi has an inverted radio spectrum and based on survey data we found a flaring radio source at the position of AT2017bgt. These findings suggest that newly ejected radio-emitting components play an important role not only in BFFs, but might be connected to the coronal line emission. A detailed radio study of other BFFs and coronal line emitters is crucial to better understand the appearance of these highly ionized lines.

Altogether, our results are consistent with the Bowen Fluorescence Flare classification of AT2019aalc. We also classify AT2019aalc as an Extreme Coronal Line Emitter. A connection between the ECLs, some TDEs and BFFs suggested by our spectroscopy results makes a non-standard TDE-related scenario more probable to explain the optical flares and i.e. the restarted activity of the host AGN. Moreover, due to the pre-existing BLR and therefore the high densities, TDE-AGN are more capable for the Bowen Fluorescence mechanism and the high-ionization coronal lines. Only a few TDEs were detected with coronal lines; these are also known as TDEs with extreme dust echo emission.

Continuous interactions of a pair of binary star and the SMBH favored by Trakhtenbrot et al. (2019) might explain the re-brightened and slowly decaying optical emission of BFFs. An alternative scenario for the two distinct optical flares is a partial disruption of a single star in an AGN. Here, the slowly decaying reprocessed optical/UV emission originates from soft X-ray flares powered by continuous tidal interaction between the stellar debris and the pre-existing accretion disk. The double-peaked optical light curve is explained with a second disruption due to the surviving core after the first passage. However, more BFFs are needed to study the mechanism responsible for these transients. TDE-related scenarios nevertheless provide an explanation not only for the suddenly enhanced activity of the nucleus but also for the high metallicity of the ionized gas. Future observations will help us to better understand the nature of the transient; a binary TDE would not produce a third flare, a repeating TDE would lead to a roughly periodic flaring, while some other AGN activity would lead to erratic future flares.

Motivated by the high-energy neutrino associated with AT2019aalc, we cross-matched the ICECAT-1 with the positions of the known 4 BFFs. We found that AT2021loi is coincident with the high-energy neutrino event IC-230511 confirming the flaring AGN-neutrino connection studied by van Velzen et al. (2024). Apart from the known multi-wavelength properties of BFFs, AT2021loi shares characteristics with AT2019aalc such as late-time IR flare (due to dust echo), high-ionization coronal lines in its spectra (and also r -band excess), radio detection (and inverted radio spectrum) and re-brightening episode/bumps in optical. In both cases the host galaxies are classified as broad-line AGN with remarkable star formation activity.

Acknowledgements

We thank Benny Trakhtenbrot for useful discussions. PMV, AF, BA, ST, AK, DJB, EM-B acknowledge the support from the DFG via the Collaborative Research Center SFB1491 *Cosmic Interacting Matters - From Source to Signal*. EH acknowledges support by NASA under award number 80GSFC21M0002.

The European VLBI Network is a joint facility of independent European, African, Asian, and North American radio astronomy institutes. Scientific results from data presented in this publication are derived from the following EVN project code: EV027. e-MERLIN is a National Facility operated by the University of Manchester at Jodrell Bank Observatory on behalf of STFC.

We acknowledge the use of public data from the Swift data archive. This research has made use of the XRT Data Analysis Software (XRTDAS) developed under the responsibility of the ASI Science Data Center (ASDC), Italy. The Australia Telescope Compact Array is part of the Australia Telescope National Facility <https://ror.org/05qajvd42> which is funded by the Australian Government for operation as a National Facility managed by CSIRO. We acknowledge the Gomeri people as the Traditional Owners of the Observatory site. Funding for the Sloan Digital Sky Survey V has been provided by the Alfred P. Sloan Foundation, the Heising-Simons Foundation, the National Science Foundation, and the Participating Institutions. SDSS acknowledges support and resources from the Center for High-Performance Computing at the University of Utah. SDSS telescopes are located at Apache Point Observatory, funded by the Astrophysical Research Consortium and operated by New Mexico State University, and at Las Campanas Observatory, operated by the Carnegie Institution for Science. The SDSS web site is www.sdss.org. SDSS is managed by the Astrophysical Research Consortium for the Participating Institutions of the SDSS Collaboration, including Caltech, The Carnegie Institution for Science, Chilean National Time Allocation Committee (CNTAC) ratified researchers, The Flatiron Institute, the Gotham Participation Group, Harvard University, Heidelberg University, The Johns Hopkins University, L'École polytechnique fédérale de Lausanne (EPFL), Leibniz-Institut für Astrophysik Potsdam (AIP), Max-Planck-Institut für Astronomie (MPIA Heidelberg), Max-Planck-Institut für Extraterrestrische Physik (MPE), Nanjing University, National Astronomical Observatories of China (NAOC), New Mexico State University, The Ohio State University, Pennsylvania State University, Smithsonian Astrophysical Observatory, Space Telescope Science Institute (STScI), the Stellar Astrophysics Participation Group, Universidad Nacional Autónoma de México, University of Arizona, University of Colorado Boulder, University of Illinois at Urbana-Champaign, University of Toronto, University of Utah, University of Virginia, Yale University, and Yunnan University. This publication makes use of data products from the Wide-field Infrared Survey Explorer, which is a joint project of the University of California, Los Angeles, and the Jet Propulsion Laboratory/California Institute of Technology, and NEOWISE, which is a project of the Jet Propulsion Laboratory/California Institute of Technology. WISE and NEOWISE are funded by the National Aeronautics and Space Administration. The National Radio Astronomy Observatory is a facility of the National Science Foundation operated under cooperative agreement by Associated Universities, Inc. This work has made use of data from the Asteroid Terrestrial-impact Last Alert System (ATLAS) project. The Asteroid Terrestrial-impact Last Alert System (ATLAS) project is primarily funded to search for near earth asteroids through NASA grants NN12AR55G, 80NSSC18K0284, and 80NSSC18K1575; byproducts of the NEO search include images and catalogs from the survey area. This work was partially funded by Kepler/K2 grant J1944/80NSSC19K0112 and HST GO-15889, and STFC grants ST/T000198/1 and ST/S006109/1. The ATLAS science products have been made possible through the contributions of the University of Hawaii Institute for Astronomy, the Queen's University Belfast, the Space Telescope Science Institute, the South African Astronomical Observatory, and The Millennium Institute of Astrophysics (MAS), Chile. This work is based on data from eROSITA, the soft X-ray instrument aboard SRG, a joint Russian-German science mission supported by the Russian Space Agency (Roskosmos), in the interests of the Russian Academy of Sciences represented

by its Space Research Institute (IKI), and the Deutsches Zentrum für Luft- und Raumfahrt (DLR). The SRG spacecraft was built by Lavochkin Association (NPOL) and its subcontractors, and is operated by NPOL with support from the Max Planck Institute for Extraterrestrial Physics (MPE). The development and construction of the eROSITA X-ray instrument was led by MPE, with contributions from the Dr. Karl Remeis Observatory Bamberg & ECAP (FAU Erlangen-Nuernberg), the University of Hamburg Observatory, the Leibniz Institute for Astrophysics Potsdam (AIP), and the Institute for Astronomy and Astrophysics of the University of Tübingen, with the support of DLR and the Max Planck Society. The Argelander Institute for Astronomy of the University of Bonn and the Ludwig Maximilians Universität Munich also participated in the science preparation for eROSITA. The Pan-STARRS1 Surveys (PS1) and the PS1 public science archive have been made possible through contributions by the Institute for Astronomy, the University of Hawaii, the Pan-STARRS Project Office, the Max-Planck Society and its participating institutes, the Max Planck Institute for Astronomy, Heidelberg and the Max Planck Institute for Extraterrestrial Physics, Garching, The Johns Hopkins University, Durham University, the University of Edinburgh, the Queen's University Belfast, the Harvard-Smithsonian Center for Astrophysics, the Las Cumbres Observatory Global Telescope Network Incorporated, the National Central University of Taiwan, the Space Telescope Science Institute, the National Aeronautics and Space Administration under Grant No. NNX08AR22G issued through the Planetary Science Division of the NASA Science Mission Directorate, the National Science Foundation Grant No. AST-1238877, the University of Maryland, Eotvos Lorand University (ELTE), the Los Alamos National Laboratory, and the Gordon and Betty Moore Foundation. These results made use of the Lowell Discovery Telescope (LDT) at Lowell Observatory. Lowell is a private, non-profit institution dedicated to astrophysical research and public appreciation of astronomy and operates the LDT in partnership with Boston University, the University of Maryland, the University of Toledo, Northern Arizona University and Yale University. The upgrade of the DeVeny optical spectrograph has been funded by a generous grant from John and Ginger Giovale and by a grant from the Mt. Cuba Astronomical Foundation. Some of the data presented herein were obtained at Keck Observatory, which is a private 501(c)3 non-profit organization operated as a scientific partnership among the California Institute of Technology, the University of California, and the National Aeronautics and Space Administration. The Observatory was made possible by the generous financial support of the W. M. Keck Foundation. The authors wish to recognize and acknowledge the very significant cultural role and reverence that the summit of Maunakea has always had within the Native Hawaiian community. We are most fortunate to have the opportunity to conduct observations from this mountain. This publication makes use of data products from the Two Micron All Sky Survey, which is a joint project of the University of Massachusetts and the Infrared Processing and Analysis Center/California Institute of Technology, funded by the National Aeronautics and Space Administration and the National Science Foundation. Based on observations obtained with the Samuel Oschin Telescope 48-inch and the 60-inch Telescope at the Palomar Observatory as part of the Zwicky Transient Facility project. ZTF is supported by the National Science Foundation under Grant No. AST-2034437 and a collaboration including Caltech, IPAC, the Weizmann Institute for Science, the Oskar Klein Center at Stockholm University, the University of Maryland, Deutsches Elektronen-Synchrotron and Humboldt Univer-

sity, the TANGO Consortium of Taiwan, the University of Wisconsin at Milwaukee, Trinity College Dublin, Lawrence Livermore National Laboratories, and IN2P3, France. Operations are conducted by COO, IPAC, and UW.

References

- Abazajian, K. N., Adelman-McCarthy, J. K., Agüeros, M. A., et al. 2009, *ApJS*, 182, 543
- Abbasi, R., Ackermann, M., Adams, J., et al. 2023, *ApJS*, 269, 25
- Acciari, V. A., Aniello, T., Ansoldi, S., et al. 2022, *ApJ*, 927, 197
- Ahn, C. P., Alexandroff, R., Allende Prieto, C., et al. 2012, *ApJS*, 203, 21
- Arnaud, K. A. 1996a, in *Astronomical Society of the Pacific Conference Series*, Vol. 101, *Astronomical Data Analysis Software and Systems V*, ed. G. H. Jacoby & J. Barnes, 17
- Arnaud, K. A. 1996b, in *Astronomical Society of the Pacific Conference Series*, Vol. 101, *Astronomical Data Analysis Software and Systems V*, ed. G. H. Jacoby & J. Barnes, 17
- Baldwin, J. A., Phillips, M. M., & Terlevich, R. 1981, *PASP*, 93, 5
- Baskin, A. & Laor, A. 2005, *MNRAS*, 358, 1043
- Behar, E., Baldi, R. D., Laor, A., et al. 2015, *MNRAS*, 451, 517
- Berger, E., Zauderer, A., Pooley, G. G., et al. 2012, *ApJ*, 748, 36
- Berk, D. E. V., Wilhite, B. C., Kron, R. G., et al. 2004, *The Astrophysical Journal*, 601, 692
- Bertero, M. & de Mol, C. 1996, *Progress in Optics*, 36, 129
- Bertin, E., Mellier, Y., Radovich, M., et al. 2002, in *Astronomical Society of the Pacific Conference Series*, Vol. 281, *Astronomical Data Analysis Software and Systems XI*, ed. D. A. Bohlender, D. Durand, & T. H. Handley, 228
- Berton, M., Järvelä, E., Crepaldi, L., et al. 2020, *A&A*, 636, A64
- Bianchi, L., Herald, J., Efreanova, B., et al. 2011, *Ap&SS*, 335, 161
- Binette, L., Zovaro, H. R. M., Villar Martín, M., et al. 2024, *A&A*, 684, A53
- Blagorodnova, N., Cenko, S. B., Kulkarni, S. R., et al. 2019, *ApJ*, 873, 92
- Blanchard, P. K., Nicholl, M., Berger, E., et al. 2017, *ApJ*, 843, 106
- Boller, T., Brandt, W. N., & Fink, H. 1996, *A&A*, 305, 53
- Bontempi, P., Giroletti, M., Panessa, F., Orienti, M., & Doi, A. 2012, *MNRAS*, 426, 588
- Bowen, I. S. 1934, *PASP*, 46, 146
- Bowen, I. S. 1935, *ApJ*, 81, 1
- Brown, G. C., Levan, A. J., Stanway, E. R., et al. 2015, *MNRAS*, 452, 4297
- Bruzual, G. & Charlot, S. 2003, *MNRAS*, 344, 1000
- Bu, D.-F., Qiao, E., Yang, X.-H., & Liu, J. 2022, *arXiv e-prints*, arXiv:2208.04118
- Burrows, D. N., Hill, J. E., Nousek, J. A., et al. 2005, *Space Sci. Rev.*, 120, 165
- Campana, S., Mainetti, D., Colpi, M., et al. 2015, *A&A*, 581, A17
- Cannizzaro, G., Wevers, T., Jonker, P. G., et al. 2021, *MNRAS*, 504, 792
- Cappellari, M. 2017, *MNRAS*, 466, 798
- Cappellari, M. 2023, *MNRAS*, 526, 3273
- Cappellari, M. & Emsellem, E. 2004, *PASP*, 116, 138
- Cardelli, J. A., Clayton, G. C., & Mathis, J. S. 1989, *ApJ*, 345, 245
- Cash, W. 1976, *A&A*, 52, 307
- Cendes, Y., Berger, E., Alexander, K. D., et al. 2023, *arXiv e-prints*, arXiv:2308.13595
- Cenko, S. B., Krimm, H. A., Horesh, A., et al. 2012, *ApJ*, 753, 77
- Cerqueira-Campos, F. C., Rodríguez-Ardila, A., Riffel, R., et al. 2021, *MNRAS*, 500, 2666
- Chambers, K. C., Magnier, E. A., Metcalfe, N., et al. 2016, *arXiv e-prints*, arXiv:1612.05560
- Chan, C.-H., Piran, T., Krolik, J. H., & Saban, D. 2019, *ApJ*, 881, 113
- Charalampopoulos, P., Leloudas, G., Malesani, D. B., et al. 2022a, *A&A*, 659, A34
- Charalampopoulos, P., Leloudas, G., Malesani, D. B., et al. 2022b, *A&A*, 659, A34
- Charalampopoulos, P., Pursiainen, M., Leloudas, G., et al. 2023, *A&A*, 673, A95
- Charlot, P., Jacobs, C. S., Gordon, D., et al. 2020, *A&A*, 644, A159
- Chatterjee, S., Cordes, J. M., Vlemmings, W. H. T., et al. 2004, *ApJ*, 604, 339
- Chen, J.-H., Dou, L.-M., & Shen, R.-F. 2022, *ApJ*, 928, 63
- Condon, J. J. 1992, *ARA&A*, 30, 575
- Condon, J. J., Condon, M. A., Gislser, G., & Puschell, J. J. 1982, *ApJ*, 252, 102
- Condon, J. J., Cotton, W. D., Greisen, E. W., et al. 1998, *AJ*, 115, 1693
- Conroy, C., Gunn, J. E., & White, M. 2009, *ApJ*, 699, 486
- Cutri, R. M., Skrutskie, M. F., van Dyk, S., et al. 2003, *2MASS All Sky Catalog of point sources*. (Infrared Processing and Analysis Center)
- Czerny, B., Siemiginowska, A., Janiak, A., Nikiel-Wroczyński, B., & Stawarz, Ł. 2009, *ApJ*, 698, 840
- De Colle, F. & Lu, W. 2020, *New A Rev.*, 89, 101538
- Dgany, Y., Arcavi, I., Makrygianni, L., Pellegrino, C., & Howell, D. A. 2023, *ApJ*, 957, 57

- Djorgovski, S. G., Drake, A. J., Mahabal, A. A., et al. 2011, arXiv e-prints, arXiv:1102.5004
- Done, C., Davis, S. W., Jin, C., Blaes, O., & Ward, M. 2012, MNRAS, 420, 1848
- Dou, L., Wang, T.-g., Jiang, N., et al. 2016, ApJ, 832, 188
- Evans, P. A., Osborne, J. P., Beardmore, A. P., et al. 2014, ApJS, 210, 8
- Fomalont, E. B. 1999, in *Astronomical Society of the Pacific Conference Series*, Vol. 180, *Synthesis Imaging in Radio Astronomy II*, ed. G. B. Taylor, C. L. Carilli, & R. A. Perley, 301
- Frederick, S., Gezari, S., Graham, M. J., et al. 2019, ApJ, 883, 31
- Frederick, S., Gezari, S., Graham, M. J., et al. 2021, ApJ, 920, 56
- French, K. D., Wevers, T., Law-Smith, J., Graur, O., & Zabludoff, A. I. 2020, *Space Sci. Rev.*, 216, 32
- French, K. D., Yang, Y., Zabludoff, A., et al. 2015, ApJ, 801, 1
- Gaia Collaboration, Vallenari, A., Brown, A. G. A., et al. 2023, A&A, 674, A1
- Gallimore, J. F., Baum, S. A., & O’Dea, C. P. 1997, *Nature*, 388, 852
- Garrington, S. T., Anderson, B., Baines, C., et al. 2004, in *Society of Photo-Optical Instrumentation Engineers (SPIE) Conference Series*, Vol. 5489, *Ground-based Telescopes*, ed. J. Oschmann, Jacobus M., 332–343
- Gelbord, J. M., Mullaney, J. R., & Ward, M. J. 2009, MNRAS, 397, 172
- Gezari, S. 2021, ARA&A, 59, 21
- Gezari, S., Martin, D. C., Forster, K., et al. 2013, ApJ, 766, 60
- Green, R. F., Schmidt, M., & Liebert, J. 1986, ApJS, 61, 305
- Greisen, E. W. 1990, in *Acquisition, Processing and Archiving of Astronomical Images*, 125–142
- Guedel, M. & Benz, A. O. 1993, ApJ, 405, L63
- Hampel, J., Komossa, S., Greiner, J., et al. 2022, *Research in Astronomy and Astrophysics*, 22, 055004
- HI4PI Collaboration, Ben Bekhti, N., Flöer, L., et al. 2016, A&A, 594, A116
- Hinkle, J. T. 2024, MNRAS, 531, 2603
- Högbom, J. A. 1974, A&AS, 15, 417
- Horesh, A., Sfaradi, I., Fender, R., et al. 2021, ApJ, 920, L5
- Hung, T., Gezari, S., Blagorodnova, N., et al. 2017, ApJ, 842, 29
- IceCube Collaboration. 2019, GRB Coordinates Network, 26258, 1
- IceCube Collaboration. 2023, GRB Coordinates Network, 33773, 1
- IceCube Collaboration, Abbasi, R., Ackermann, M., et al. 2022, *Science*, 378, 538
- Ilić, D., Kovačević, J., & Popović, L. Č. 2009, *New A Rev.*, 53, 149
- Ivezić, Ž., Connolly, A., Vanderplas, J., & Gray, A. 2014, *Statistics, Data Mining and Machine Learning in Astronomy* (Princeton University Press)
- Jansen, F., Lumb, D., Altieri, B., et al. 2001, A&A, 365, L1
- Järvelä, E., Berton, M., & Crepaldi, L. 2021, *Frontiers in Astronomy and Space Sciences*, 8, 147
- Ji, X., Maiolino, R., Ferland, G., et al. 2024, arXiv e-prints, arXiv:2405.05772
- Johnson, B. & Leja, J. 2017, *bd-j/prospector: Initial release*
- Jones, D. H., Read, M. A., Saunders, W., et al. 2009, MNRAS, 399, 683
- Kammoun, E. S., Papadakis, I. E., & Sabra, B. M. 2015, A&A, 582, A40
- Keimpema, A., Kettenis, M. M., Pogrebenko, S. V., et al. 2015, *Experimental Astronomy*, 39, 259
- Kewley, L. J., Dopita, M. A., Sutherland, R. S., Heisler, C. A., & Trevena, J. 2001, ApJ, 556, 121
- Kharb, P., Das, M., Paragi, Z., Subramanian, S., & Chitta, L. P. 2015, ApJ, 799, 161
- Koay, J. Y., Vestergaard, M., Bignall, H. E., Reynolds, C., & Peterson, B. M. 2016, MNRAS, 460, 304
- Kochanek, C. S., Shappee, B. J., Stanek, K. Z., et al. 2017, PASP, 129, 104502
- Koljonen, K. I. I., Liodakis, I., Lindfors, E., et al. 2024, MNRAS, 532, 112
- Kovalev, Y. Y., Kellermann, K. I., Lister, M. L., et al. 2005, AJ, 130, 2473
- Kozák, B., Frey, S., & Gabányi, K. É. 2024, *Galaxies*, 12, 8
- Kraemer, S. B. & Crenshaw, D. M. 2000, ApJ, 544, 763
- Kroupa, P. 2001, MNRAS, 322, 231
- Lacy, M., Baum, S. A., Chandler, C. J., et al. 2020, PASP, 132, 035001
- Laor, A. & Behar, E. 2008, MNRAS, 390, 847
- Law, N. M., Kulkarni, S. R., Dekany, R. G., et al. 2009, PASP, 121, 1395
- Leloudas, G., Dai, L., Arcavi, I., et al. 2019, ApJ, 887, 218
- Lin, Z., Jiang, N., Wang, T., et al. 2024, arXiv e-prints, arXiv:2405.10895
- Liu, H.-Y., Liu, W.-J., Dong, X.-B., et al. 2019, ApJS, 243, 21
- Liu, Z., Malyali, A., Krumpke, M., et al. 2023, A&A, 669, A75
- Lobanov, A. 2015, A&A, 574, A84
- Lu, W., Kumar, P., & Evans, N. J. 2016, MNRAS, 458, 575
- Maddox, N. 2018, MNRAS, 480, 5203
- Mahadevan, R. 1997, ApJ, 477, 585
- Mainzer, A., Bauer, J., Grav, T., et al. 2011, ApJ, 731, 53
- Makrygianni, L., Trakhtenbrot, B., Arcavi, I., et al. 2023, ApJ, 953, 32
- Malkan, M. A. 1986, ApJ, 310, 679
- Malyali, A., Rau, A., Merloni, A., et al. 2021, A&A, 647, A9
- Mandel, I. & Levin, Y. 2015, ApJ, 805, L4
- Mandigo-Stoba, M. S., Fremling, C., & Kasliwal, M. 2022, *The Journal of Open Source Software*, 7, 3612
- Martin, D. C., Fanson, J., Schiminovich, D., et al. 2005, ApJ, 619, L1
- Masci, F. J., Laher, R. R., Rusholme, B., et al. 2023, arXiv e-prints, arXiv:2305.16279
- Masci, F. J., Laher, R. R., Rusholme, B., et al. 2019, PASP, 131, 018003
- Mazzalay, X., Rodríguez-Ardila, A., & Komossa, S. 2010, MNRAS, 405, 1315
- Mazzolari, G., Übler, H., Maiolino, R., et al. 2024, arXiv e-prints, arXiv:2404.10811
- McConnell, D., Hale, C. L., Lenc, E., et al. 2020, PASA, 37, e048
- Million, C., Fleming, S. W., Shiao, B., et al. 2016, ApJ, 833, 292
- Mohan, P., An, T., Zhang, Y., et al. 2022, ApJ, 927, 74
- Mundell, C. G., Ferruit, P., Nagar, N., & Wilson, A. S. 2009, ApJ, 703, 802
- Nagao, T., Murayama, T., & Taniguchi, Y. 2001, ApJ, 549, 155
- Nagao, T., Taniguchi, Y., & Murayama, T. 2000, AJ, 119, 2605
- Necker, J., Graikou, E., Kowalski, M., et al. 2024, arXiv e-prints, arXiv:2407.01039
- Necker, J. & Mechbal, S. 2024, *JannisNe/Timewise: V0.4.10*, Zenodo
- Netzer, H. 1990, in *Active Galactic Nuclei*, ed. R. D. Blandford, H. Netzer, L. Woltjer, T. J. L. Courvoisier, & G. Mayor, 57–160
- Netzer, H., Elitzur, M., & Ferland, G. J. 1985, ApJ, 299, 752
- Newsome, M., Arcavi, I., Dgany, Y., & Pellegrino, C. 2022, *Transient Name Server AstroNote*, 236, 1
- Nicholl, M., Wevers, T., Oates, S. R., et al. 2020, MNRAS, 499, 482
- Oh, K., Choi, H., Kim, H.-G., Moon, J.-S., & Yi, S. K. 2013, AJ, 146, 151
- Oh, K., Koss, M. J., Ueda, Y., et al. 2022, ApJS, 261, 4
- Oke, J. B. 1974, ApJS, 27, 21
- Oke, J. B., Cohen, J. G., Carr, M., et al. 1995, PASP, 107, 375
- Oke, J. B. & Gunn, J. E. 1982, PASP, 94, 586
- Oke, J. B. & Sargent, W. L. W. 1968, ApJ, 151, 807
- Oliva, E. 1997, in *Astronomical Society of the Pacific Conference Series*, Vol. 113, *IAU Colloq. 159: Emission Lines in Active Galaxies: New Methods and Techniques*, ed. B. M. Peterson, F.-Z. Cheng, & A. S. Wilson, 288
- Onori, F., Cannizzaro, G., Jonker, P. G., et al. 2022, MNRAS, 517, 76
- Oshlack, A. Y. K. N., Webster, R. L., & Whiting, M. T. 2001, ApJ, 558, 578
- Padovani, P., Alexander, D. M., Assef, R. J., et al. 2017, A&A Rev., 25, 2
- Pakull, M. W. & Angebault, L. P. 1986, *Nature*, 322, 511
- Pan, Y. C., Foley, R. J., Jha, S. W., Rest, A., & Scolnic, D. 2018, *Transient Name Server Classification Report*, 2018-998, 1
- Paragi, Z., Yang, J., Komossa, S., et al. 2017, in *New Frontiers in Black Hole Astrophysics*, ed. A. Gomboc, Vol. 324, 119–122
- Pasham, D. 2023, *The Astronomer’s Telegram*, 16118, 1
- Payne, A. V., Shappee, B. J., Hinkle, J. T., et al. 2021, ApJ, 910, 125
- Pearson, T. J. 1995, in *Astronomical Society of the Pacific Conference Series*, Vol. 82, *Very Long Baseline Interferometry and the VLBA*, ed. J. A. Zensus, P. J. Diamond, & P. J. Napier, 267
- Perley, D. A. 2019, PASP, 131, 084503
- Piran, T., Svirski, G., Krolik, J., Cheng, R. M., & Shikawa, H. 2015, ApJ, 806, 164
- Pol, N. & Wadadekar, Y. 2017, MNRAS, 465, 95
- Pons, E. & Watson, M. G. 2014, A&A, 568, A108
- Prochaska, J., Hennawi, J., Westfall, K., et al. 2020, *The Journal of Open Source Software*, 5, 2308
- Rees, M. J. 1988, *Nature*, 333, 523
- Reid, M. J., Schneps, M. H., Moran, J. M., et al. 1988, ApJ, 330, 809
- Reusch, S., Stein, R., Kowalski, M., et al. 2022, *Phys. Rev. Lett.*, 128, 221101
- Roming, P. W. A., Kennedy, T. E., Mason, K. O., et al. 2005, *Space Sci. Rev.*, 120, 95
- Ryu, T., McKernan, B., Ford, K. E. S., et al. 2024, MNRAS, 527, 8103
- Santoro, F., Tadhunter, C., Baron, D., Morganti, R., & Holt, J. 2020, A&A, 644, A54
- Sault, R. J., Teuben, P. J., & Wright, M. C. H. 1995, in *Astronomical Society of the Pacific Conference Series*, Vol. 77, *Astronomical Data Analysis Software and Systems IV*, ed. R. A. Shaw, H. E. Payne, & J. J. E. Hayes, 433
- Saxton, R., Komossa, S., Auchettl, K., & Jonker, P. G. 2020, *Space Sci. Rev.*, 216, 85
- Schachter, J., Filippenko, A. V., & Kahn, S. M. 1990, ApJ, 362, 74
- Schaerer, D., Fragos, T., & Izotov, Y. I. 2019, A&A, 622, L10
- Schlafly, E. F. & Finkbeiner, D. P. 2011, ApJ, 737, 103
- Selvelli, P., Danziger, J., & Bonifacio, P. 2007, A&A, 464, 715
- Shappee, B. J., Prieto, J. L., Grupe, D., et al. 2014, ApJ, 788, 48
- Shepherd, M. C., Pearson, T. J., & Taylor, G. B. 1994, in *Bulletin of the American Astronomical Society*, Vol. 26, 987–989
- Shirazi, M. & Brinchmann, J. 2012, MNRAS, 421, 1043
- Short, P., Lawrence, A., Nicholl, M., et al. 2023, MNRAS, 525, 1568
- Shu, X. W., Wang, S. S., Dou, L. M., et al. 2018, ApJ, 857, L16
- Smith, K. W., Smartt, S. J., Young, D. R., et al. 2020, PASP, 132, 085002
- Somalwar, J. J., Ravi, V., Dong, D., et al. 2022, ApJ, 929, 184
- Somalwar, J. J., Ravi, V., Yao, Y., et al. 2023, arXiv e-prints, arXiv:2310.03782
- Soraisam, M., Matheson, T., Lee, C.-H., et al. 2022, ApJ, 926, L11
- Stein, R., Reusch, S., Franckowiak, A., et al. 2023, MNRAS, 521, 5046
- Stein, R., van Velzen, S., Kowalski, M., et al. 2021, *Nature Astronomy*, 5, 510

- Stern, D., Assef, R. J., Benford, D. J., et al. 2012, *The Astrophysical Journal*, 753, 30
- Stern, D., Assef, R. J., Benford, D. J., et al. 2012, *ApJ*, 753, 30
- Sunyaev, R., Arefiev, V., Babushkin, V., et al. 2021, *A&A*, 656, A132
- Tadhunter, C., Patel, M., & Mullaney, J. 2021, *MNRAS*, 504, 4377
- Tonry, J. L., Denneau, L., Heinze, A. N., et al. 2018, *PASP*, 130, 064505
- Trakhtenbrot, B., Arcavi, I., Ricci, C., & Burke, J. 2020, *Transient Name Server AstroNote*, 105, 1
- Trakhtenbrot, B., Arcavi, I., Ricci, C., et al. 2019, *Nature Astronomy*, 3, 242
- Trump, J. R., Hsu, A. D., Fang, J. J., et al. 2013, *ApJ*, 763, 133
- Übler, H., Maiolino, R., Pérez-González, P. G., et al. 2024, *MNRAS*, 531, 355
- Ulvestad, J. S., Antonucci, R. R. J., & Barvainis, R. 2005, *ApJ*, 621, 123
- van Velzen, S., Gezari, S., Hammerstein, E., et al. 2021a, *ApJ*, 908, 4
- van Velzen, S., Pasham, D. R., Komossa, S., Yan, L., & Kara, E. A. 2021b, *Space Sci. Rev.*, 217, 63
- van Velzen, S., Stein, R., Gilfanov, M., et al. 2024, *MNRAS*, 529, 2559
- Vanden Berk, D. E., Richards, G. T., Bauer, A., et al. 2001, *AJ*, 122, 549
- Vanderplas, J., Connolly, A., Ivezić, Ž., & Gray, A. 2012, in *Conference on Intelligent Data Understanding (CIDU)*, 47–54
- Veres, P. M., Reusch, S., Stein, R., et al. 2023, *Transient Name Server AstroNote*, 194, 1
- Wang, Q. & Kron, R. G. 2020, *MNRAS*, 498, 4550
- Wang, T.-G., Zhou, H.-Y., Komossa, S., et al. 2012, *ApJ*, 749, 115
- Wevers, T., Coughlin, E. R., Pasham, D. R., et al. 2023, *ApJ*, 942, L33
- Wevers, T., Pasham, D. R., van Velzen, S., et al. 2019a, *MNRAS*, 488, 4816
- Wevers, T., Pasham, D. R., van Velzen, S., et al. 2019b, *MNRAS*, 488, 4816
- White, R. L., Becker, R. H., Helfand, D. J., & Gregg, M. D. 1997, *ApJ*, 475, 479
- Wilson, J. C., Eikenberry, S. S., Henderson, C. P., et al. 2003, in *Society of Photo-Optical Instrumentation Engineers (SPIE) Conference Series*, Vol. 4841, *Instrument Design and Performance for Optical/Infrared Ground-based Telescopes*, ed. M. Iye & A. F. M. Moorwood, 451–458
- Winter, W. & Lunardini, C. 2023, *ApJ*, 948, 42
- Wright, E. L. 2006, *PASP*, 118, 1711
- Wright, E. L., Eisenhardt, P. R. M., Mainzer, A. K., et al. 2010, *AJ*, 140, 1868
- Wu, H.-J., Mou, G., Wang, K., Wang, W., & Li, Z. 2022, *MNRAS*, 514, 4406
- Xiang, L., Stanghellini, C., Dallacasa, D., & Haiyan, Z. 2002, *A&A*, 385, 768
- Yao, Y., Lu, W., Harrison, F., et al. 2023a, *arXiv e-prints*, arXiv:2308.09834
- Yao, Y., Ravi, V., Gezari, S., et al. 2023b, *ApJ*, 955, L6
- Yi, I. & Boughn, S. P. 1998, *ApJ*, 499, 198
- York, D. G., Adelman, J., Anderson, Jr., J. E., et al. 2000, *AJ*, 120, 1579
- Yu, Z., Kochanek, C. S., Mathur, S., et al. 2022, *MNRAS*, 515, 5198
- Zabludoff, A., Arcavi, I., LaMassa, S., et al. 2021, *Space Sci. Rev.*, 217, 54
- Zhang, F., Shu, X., Sun, L., et al. 2022, *ApJ*, 938, 43